2019

Microglia drive APOE-dependent neurodegeneration in a tauopathy mouse model

Yang Shi
Washington University School of Medicine in St. Louis

Melissa Manis
Washington University School of Medicine in St. Louis

Justin Long
Washington University School of Medicine in St. Louis

Kairuo Wang
Washington University School of Medicine in St. Louis

Patrick M. Sullivan
Duke University

See next page for additional authors

Recommended Citation

Shi, Yang; Manis, Melissa; Long, Justin; Wang, Kairuo; Sullivan, Patrick M.; Remolina Serrano, Javier; Hoyle, Rosa; and Holtzman, David M., ,"Microglia drive APOE-dependent neurodegeneration in a tauopathy mouse model." Journal of Experimental Medicine.,. . (2019).
https://digitalcommons.wustl.edu/open_access_pubs/8467

Authors

Yang Shi, Melissa Manis, Justin Long, Kairuo Wang, Patrick M. Sullivan, Javier Remolina Serrano, Rosa Hoyle, and David M. Holtzman

JEM Journal of Experimental Medicine

ARTICLE

Microglia drive APOE-dependent neurodegeneration in a tauopathy mouse model

Yang Shi[1], Melissa Manis[1], Justin Long[1], Kairuo Wang[1], Patrick M. Sullivan[2], Javier Remolina Serrano[1], Rosa Hoyle[1], and David M. Holtzman[1]

Chronic activation of brain innate immunity is a prominent feature of Alzheimer's disease (AD) and primary tauopathies. However, to what degree innate immunity contributes to neurodegeneration as compared with pathological protein-induced neurotoxicity, and the requirement of a particular glial cell type in neurodegeneration, are still unclear. Here we demonstrate that microglia-mediated damage, rather than pathological tau-induced direct neurotoxicity, is the leading force driving neurodegeneration in a tauopathy mouse model. Importantly, the progression of ptau pathology is also driven by microglia. In addition, we found that *APOE*, the strongest genetic risk factor for AD, regulates neurodegeneration predominantly by modulating microglial activation, although a minor role of apoE in regulating ptau and insoluble tau formation independent of its immunomodulatory function was also identified. Our results suggest that therapeutic strategies targeting microglia may represent an effective approach to prevent disease progression in the setting of tauopathy.

Introduction

Alzheimer's disease (AD) is characterized by two types of pathologies: 1) misfolded, aggregated proteins (in particular, intraneuronal tau pathology) that are capable of inducing direct neurotoxicity; and 2) chronic activation of the brain's innate immune system that may induce neurodegeneration via various mechanisms, such as neuronal phagoptosis by microglia, complement-mediated neuronal damage, cytokine or reactive oxygen species–induced cell toxicity, etc. (Shi and Holtzman, 2018). However, to what degree innate immunity contributes to neurodegeneration as compared with tau-induced cell-autonomous neurotoxicity is unknown. *APOE*, the strongest genetic risk factor for late-onset AD, encodes apolipoprotein E (apoE), which by itself is a potent immune modulator (Vitek et al., 2009; Zhu et al., 2012; Gale et al., 2014; Krasemann et al., 2017; Shi et al., 2017), implying a critical role of brain innate immunity in AD pathogenesis.

We recently reported that apoE strongly regulates neurodegeneration in the setting of a tauopathy (Shi et al., 2017). The presence of apoE, particularly apoE4, significantly exacerbated neurodegeneration in P301S mice, whereas genetic ablation of murine *Apoe* was strongly neuroprotective. These effects are in part due to apoE impacting glial function, in addition to its potential direct regulation of tau pathogenesis (Shi et al., 2017). However, to what extent apoE regulates neurodegeneration via its immunomodulatory function, and which glial cell types are involved in this process, are still elusive. While both microglia and astrocytes are immune competent, accumulating genetic and functional evidence suggests that microglia, the brain-resident professional immune cells, may play a major role in regulating innate immunity-induced neurodegeneration (Leyns et al., 2017; Pimenova et al., 2018). A recent study shows that apoE cell-autonomously regulates microglial activation (Krasemann et al., 2017). *Apoe* deletion from microglia prevented microglia from acquiring a neurodegenerative phenotype that was required for neuronal cell death in a facial nerve axotomy model. This highlights a role of microglia in neurodegeneration and suggests that apoE functioning through microglia constitutes an essential mechanism regulating neurodegeneration, at least in an acute axotomy model. To understand the role of microglia in neurodegeneration in neurodegenerative diseases and how it is linked to apoE function, we depleted microglia in P301S tau transgenic mice that are homozygous for human *APOE4* (TE4) or with no expression of *Apoe* (TEKO) from 6 to 9.5 mo of age, a critical time window when neurodegeneration occurs in this mouse model. We identified a critical role of microglia in driving both neurodegeneration and tau pathogenesis, as well as in mediating apoE's effect on neurodegeneration.

---

[1]Department of Neurology, Hope Center for Neurological Disorders, Charles F. and Joanne Knight Alzheimer's Disease Research Center, Washington University School of Medicine, St. Louis, MO; [2]Department of Medicine, Duke University School of Medicine, Durham, NC.

Correspondence to David M. Holtzman: holtzman@neuro.wustl.edu.

Rockefeller University Press
J. Exp. Med. 2019 Vol. 216 No. 11 2546–2561
https://doi.org/10.1084/jem.20190980

Results

Chow formula and mouse sex affect microglial depletion efficiency by PLX3397

To deplete microglia, we used PLX3397, a selective CSF1R/c-kit/FLT3 inhibitor that has been shown to readily cross the blood brain barrier and eliminate microglia via oral delivery in mouse chow (Elmore et al., 2014). We initially formulated PLX3397 in a grain-based chow (Purina 5053) that has been used for our previous research. However, we found a strong chow- and sex-dependent effect on the drug efficiency in depleting microglia. PLX3397 supplemented in grain-based Purina 5053 showed a significantly lower efficiency in depleting microglia compared with PLX3397 supplemented in a purified ingredient chow (AIN-76A) that has been used in previous PLX3397 research (Fig. S1, A and B). Additionally, male mice showed a higher level of microglial reduction than females when treated with the same chow (AIN-76A; Fig. S1, A and B). These effects appeared to be caused by different levels of PLX3397 in the plasma, as plasma PLX3397 levels strongly correlated with the degree of microglial reduction in the brain (Fig. S1, C and D). We therefore selected AIN-76A chow and used only male mice for the study. To guarantee that we achieved complete microglial ablation, we formulated the chow with a higher concentration of PLX3397 (400 mg/kg) as compared with the previously reported concentration (290 mg/kg). The higher drug concentration resulted in highly efficient microglial depletion, with 7-d treatment eliminating ~90% of microglia and 21-d treatment eliminating virtually all microglia (Fig. S2).

Microglial ablation during a critical time window of neurodegeneration development completely blocks neurodegeneration

We treated 6-mo-old (186 d) TE4 and TEKO mice as well as their aged matched non-tau transgenic littermates with control or PLX3397-supplemented AIN-76A chow for 3 mo (99 d), and collected mouse brains at 9.5 mo of age (285 d). Consistent with our previous findings, TE4 mice treated with control chow showed severe brain atrophy predominantly in the hippocampus, piriform/entorhinal cortex, and amygdala, accompanied by significant dilatation of the lateral ventricle (Fig. 1). In contrast, TEKO mice were largely protected from tissue loss and showed preserved brain volume (Fig. 1). Strikingly, when microglia were depleted in TE4 mice for merely 3 mo, specifically during the stage when neurodegeneration begins and rapidly deteriorates, neurodegeneration was virtually fully blocked, and the brain volume of these mice remained the same as that of non-tau transgenic mice (Fig. 1). This strongly suggests that microglia are the driving force of neurodegeneration and disease progression in this tauopathy mouse model.

ApoE regulates neurodegeneration in P301S mice predominantly by regulating microglia-mediated innate immune response

As we had described previously (Shi et al., 2017), TEKO mice consistently showed a marked reduction of brain atrophy compared with TE4 mice (Fig. 1). While there was a slight trend, PLX3397-treated TEKO mice did not show a significantly increased brain volume compared with control TEKO mice (Fig. 1). The similar protective effects of microglial depletion and *Apoe* deletion on neurodegeneration suggest that apoE and microglia may function in the same axis in regulating neurodegeneration. Intriguingly, by depleting microglia, the effect of apoE on neurodegeneration was abolished, with PLX3397-treated TE4 and TEKO mice showing equal brain volumes (Fig. 1). This suggests that the effect of apoE on neurodegeneration is predominantly mediated by its immunomodulatory property in regulating microglial functions. However, this does not exclude the possibility that apoE directly regulates tau pathogenesis.

ApoE deficiency leads to a higher resistance of microglia to PLX3397-induced cell death and keeps the surviving microglia in a homeostatic state

To confirm microglial depletion in PLX3397-treated mice, we stained mouse brain sections with ionized calcium binding adaptor molecule 1 (Iba1) to assess the total microglia population. We found that PLX3397 treatment resulted in ~100% microglial depletion in nearly all TE4 and E4 mice throughout the brain (Fig. 2, A and B), with only a few TE4 mice retaining a small pool of microglia in the piriform/entorhinal cortex and even sparser microglia in the hippocampus (Fig. 2 D). These Iba1$^+$ microglia almost invariably co-localized with a microglial activation marker, cluster of differentiation 68 (CD68; Fig. 2 E), indicating an activated status. A previous study showed that *Csf1r* expression is down-regulated in activated microglia in neurodegenerative conditions (Krasemann et al., 2017), suggesting that activated microglia are less dependent on the CSF1R signaling pathway, and therefore may be less susceptible to apoptosis induced by blockage of CSF1R signaling. Interestingly, in addition to sparse Iba1$^+$CD68$^+$ microglia in the gray matter, there were also significant CD68$^+$Iba1$^-$ signals in the white matter, particularly in the fimbria (Fig. 2 E), suggesting two different types of activated microglia in the hippocampus. The retention of CD68$^+$ microglia in these drug-treated TE4 mice correlated with a higher level of neurodegeneration in respective brain regions (Fig. 2 F), suggesting a linkage between activated microglia and neurodegeneration.

Interestingly, *Apoe* ablation, particularly in the presence of the tau transgene, increased microglial resistance to PLX3397-induced cell death, resulting in a higher retention of Iba1$^+$ microglia not only in the hippocampus and piriform/entorhinal cortex, but also occasionally in other brain regions such as thalamus (Fig. 2, A and C). However, unlike surviving microglia in TE4 mice, the remaining microglia in TEKO mice were largely negative for CD68 (Fig. 2 G), indicating maintenance of a homeostatic status. The enhanced survival of nonactivated microglia in *Apoe*-deficient mice suggests that apoE regulates CSF1R signaling in microglia and likely affects downstream functions such as cell survival, proliferation, and differentiation. *Apoe* ablation may reprogram microglia to be less dependent on CSF1R signaling or raise the threshold for microglial apoptosis by up-regulating CSF1R expression. Therefore, microglial preservation in TE4 and TEKO mice upon PLX3397 treatment likely followed two distinct mechanisms. The retention of nonactivated

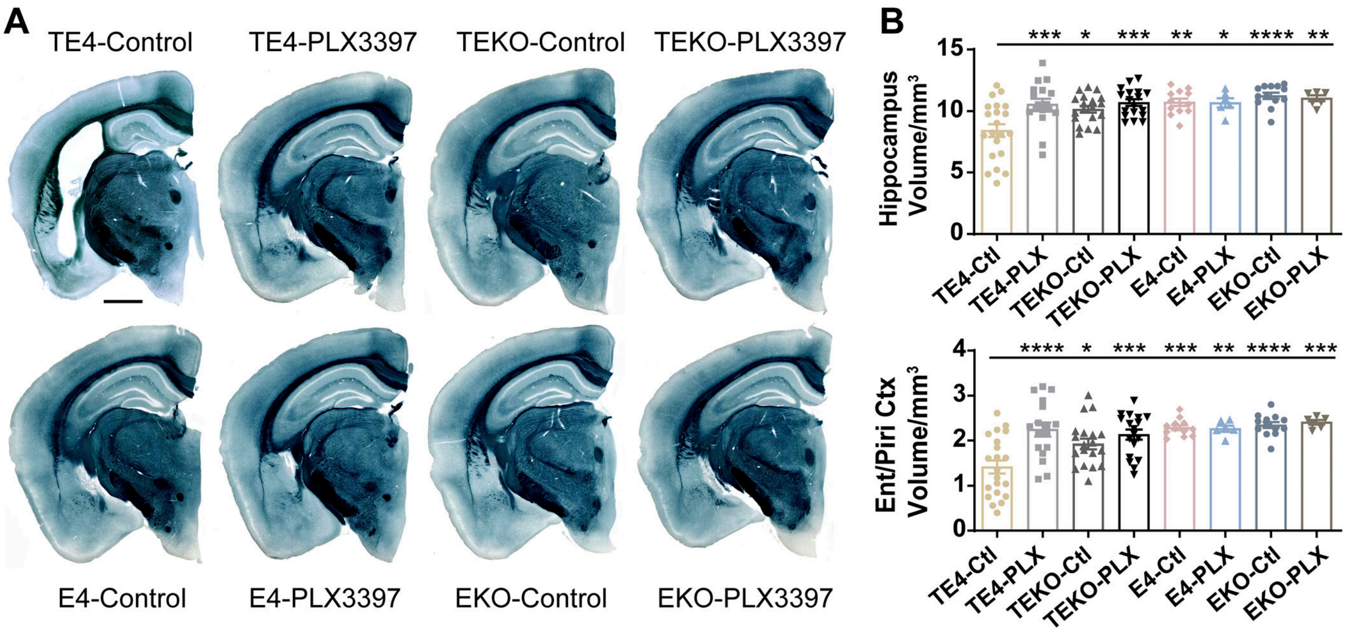

Figure 1. **Microglial depletion fully rescues neurodegeneration in TE4 mice and eliminates apoE's effect on neurodegeneration. (A)** Representative images of mouse brain sections stained with Sudan black for 9.5-mo-old TE4, TEKO, E4, and EKO mice treated with control or PLX3397-supplemented chow. Scale bar = 1 mm for all images. **(B)** Quantification of brain volumes in the hippocampus and the piriform/entorhinal cortex (Ent/Piri Ctx) of the mice (TE4-Ctl: $n = 21$; TE4-PLX: $n = 17$; TEKO-Ctl: $n = 19$; TEKO-PLX: $n = 18$; E4-Ctl: $n = 12$; E4-PLX: $n = 6$; EKO-Ctl: $n = 13$; EKO-PLX: $n = 6$). Data are expressed as means ± SEM. One-way ANOVA with Tukey's post hoc test (two-sided) was used for statistical analyses. *, $P < 0.05$; **, $P < 0.01$; ***, $P < 0.001$; ****, $P < 0.0001$. The Sudan black staining and brain volume quantification was performed once.

microglia in TEKO mice is likely due to an intrinsically higher resistance to or a higher tolerance of PLX3397-induced apoptosis by apoE-deficient microglia, whereas the CD68$^+$ microglia retained in TE4 mice likely came from enhanced survival of microglia that had been activated before PLX3397 treatment, owing to the accelerated disease progression in TE4 mice. The dissociation between Iba1 and CD68 signals in PLX3397-treated TEKO mice was most prominent in the hippocampus, where >95% of remaining Iba1$^+$ microglia were CD68 negative, whereas in the piriform/entorhinal cortex, a higher and more variable degree of co-localization was observed (Fig. 2 G). The emerging CD68$^+$ microglia in PLX3397-treated TEKO mice was most likely due to chronic activation of the initially surviving nonactivated microglia during disease progression at a later stage. The variation of the CD68$^+$ microglia levels between the hippocampus and piriform/entorhinal cortex indicates relatively independent disease progression in these two brain regions, with the piriform/entorhinal cortex appearing to be affected earlier than the hippocampus.

The activation status of microglia, but not the proliferation of microglia, is associated with neurodegeneration

Interestingly, we observed no difference in the percent area covered by Iba1 immunoreactivity between TE4 and TEKO mice treated with the control chow (Fig. 2, A and B), despite a significant difference of brain volume between these mice. In contrast, there was a significant reduction of CD68 immunoreactivity in control chow-treated TEKO mice compared with TE4 mice (Fig. 3, A and B). Furthermore, the amount of CD68 immunoreactivity highly correlated with the degree of brain atrophy (Fig. 3 C). This supports the idea that the activation status of microglia, but not their absolute number, determines microglial neurodegenerative functions. On the other hand, we observed no difference in the level of glial fibrillary acidic protein (GFAP)$^+$ astrocytes in TE4 and TEKO mice treated with either control or PLX3397-supplemented chow (Fig. S3), suggesting that the number of GFAP$^+$ astrocytes is not directly linked with neurodegeneration.

Microglia are the driving force of tau pathogenesis and mediate apoE's effect on tau pathology

Microglial activation has been shown to promote tau phosphorylation by activating tau kinases via IL-1 signaling (Li et al., 2003; Kitazawa et al., 2005). To understand how tau pathology develops with little to no impact of microglia and how apoE regulates tau pathogenesis independent of its effect on microglia, we analyzed tau pathology in mouse brains. We first stained brain sections with the AT8 antibody that recognizes the Ser202 and Thr205 epitopes of phosphorylated tau (ptau). We previously identified four types of ptau staining patterns (type1–type4) in P301S tau transgenic mice that are associated with progressively more advanced pathological tau/neurodegeneration stages (Shi et al., 2017). Consistent with our previous findings, TEKO mice treated with control chow were highly enriched with the type1 pattern, which represents the earliest pathological tau stage, whereas TE4 mice treated with control chow showed predominantly type3 and type4 patterns, which are associated with advanced tau stages and neurodegeneration (Fig. 4, A and B). Remarkably, microglial depletion in TE4 mice from 6 mo of age, a time point shortly after tau

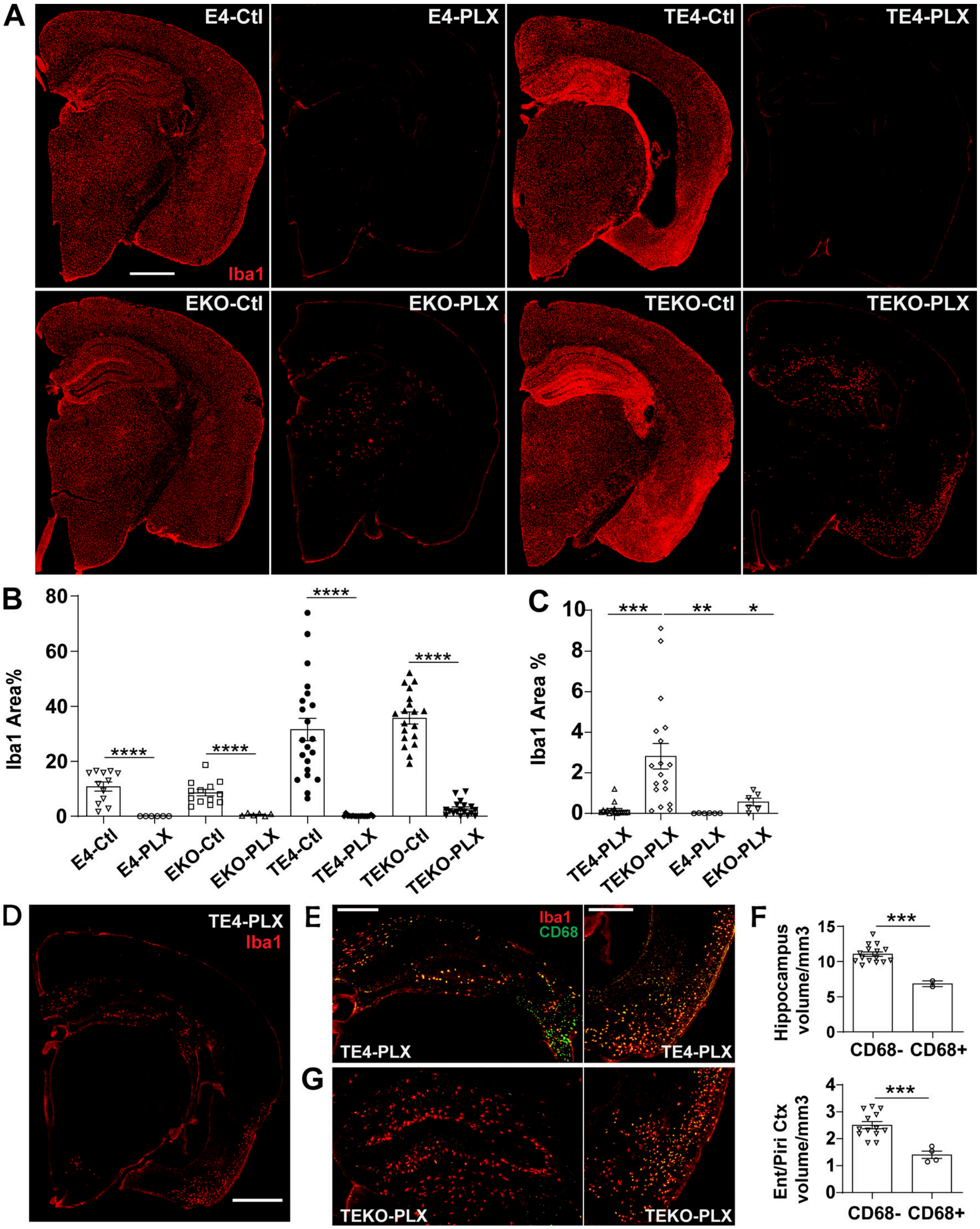

Figure 2. **ApoE deficiency increases homeostatic microglial survival in PLX3397 treatment. (A)** Representative images of Iba1 staining for 9.5-mo-old TE4, TEKO, E4, and EKO mice treated with control (Ctl) or PLX3397-supplemented (PLX) chow. Scale bar = 1 mm for all images. **(B)** Quantification of Iba1-covered areas in these brain sections (TE4-Ctl: *n* = 21; TE4-PLX: *n* = 17; TEKO-Ctl: *n* = 19; TEKO-PLX: *n* = 18; E4-Ctl: *n* = 12; E4-PLX: *n* = 6; EKO-Ctl: *n* = 13; EKO-PLX: *n* = 6). **(C)** Quantification of Iba1-covered area in PLX3397-treated mice alone. **(D)** A representation image of a TE4 mouse that showed incomplete microglial depletion in the brain. Scale bar = 1 mm. **(E)** Co-localization of Iba1 and CD68 signals in the surviving microglia in the hippocampus and entorhinal/piriform cortex (Ent/Piri Ctx) of a TE4 mouse. Scale bar = 500 µm. **(F)** The presence of surviving $CD68^+$ microglia in some PLX3397-treated TE4 mice was associated with higher levels of neurodegeneration in the hippocampus and entorhinal/piriform cortex. **(G)** The surviving microglia in PLX3397-treated TEKO mice were predominantly $CD68^-$ in the hippocampus, but showed a higher degree of co-localization with CD68 in the entorhinal/piriform cortex. Hippocampus and piriform/entorhinal cortex share the same scale with the respective regions in E. *, $P < 0.05$; **, $P < 0.01$; ***, $P < 0.001$; ****, $P < 0.0001$. The fluorescent stainings were performed once.

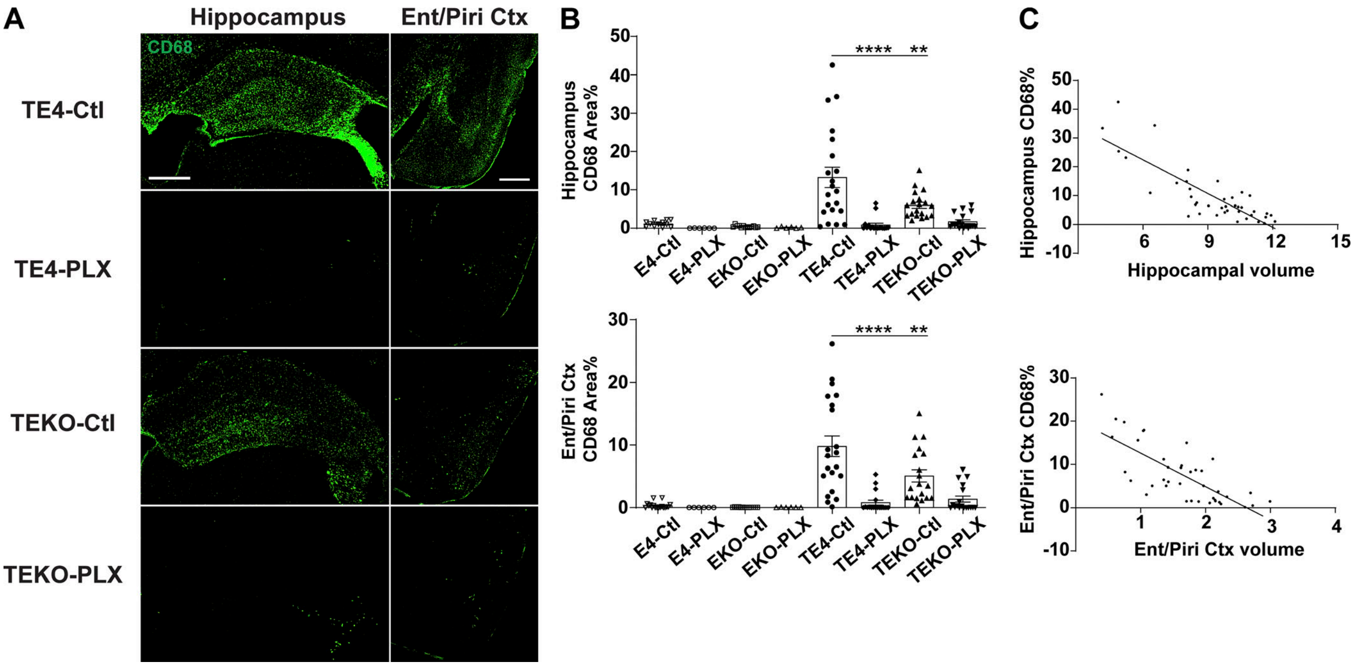

Figure 3. **Activated microglia are associated with neurodegeneration. (A)** Representative images of CD68 staining in the hippocampus and entorhinal/piriform cortex (Ent/Piri Ctx) of 9.5-mo-old TE4 and TEKO mice treated with control (Ctl) or PLX3397-supplemented (PLX) chow. Scale bar = 500 µm. Images of the same brain region share the same scale. **(B)** Quantification of CD68-covered area in all groups of mice (TE4-Ctl: $n = 21$; TE4-PLX: $n = 17$; TEKO-Ctl: $n = 19$; TEKO-PLX: $n = 18$; E4-Ctl: $n = 12$; E4-PLX: $n = 6$; EKO-Ctl: $n = 13$; EKO-PLX: $n = 6$). **(C)** Correlation between CD68 signal and the brain volume in the hippocampus and entorhinal/piriform cortex in control TE4 and TEKO mice. Pearson correlation analysis (two-sided). Hippocampus: $R^2 = 0.6872$, $P < 0.0001$; entorhinal/piriform cortex: $R^2 = 0.5611$, $P < 0.0001$. Data are expressed as means ± SEM. One-way ANOVA with Tukey's post hoc test. **, $P < 0.01$; ****, $P < 0.0001$. The CD68 staining was performed once.

pathology onset, completely blocked the progression of pathological tau stages, resulting in almost exclusively a type1 pattern in these mice (Fig. 4 B). This result strongly indicates that microglia are the primary driving force of ptau histopathology. Activated microglia either directly induce tau hyperphosphorylation by activating tau kinases through IL-1 or other signaling pathways, or trigger neurodegeneration that leads to secondary tau hyperphosphorylation and aggregation as a consequence of neuronal injury. Microglial depletion in TEKO mice did not further change the ptau staining pattern as compared with TEKO control mice, as both groups showed similar enrichment of type1 tau (Fig. 4 B). Quantification of AT8 immunoreactivity in the hippocampus revealed a significant ptau reduction in PLX3397-treated TE4 mice compared with control TE4 mice, with no difference noted between PLX3397-treated and control TEKO mice (Fig. 4 C). However, we noticed that type1 tau exhibited two sub-categories: an early-type1 stage characterized by solely mossy fiber staining and a late-type1 stage featuring emerging neuronal cell body and neuritic staining in addition to mossy fiber staining (Fig. 4 D). We found that control TEKO mice demonstrated a significant shift from the early-type1 tau toward the late subtype relative to PLX3397-treated TEKO mice (Fig. 4 E), indicating a mildly accelerated rate of disease progression. Notably, in the absence of microglia, TE4 and TEKO mice showed comparable degrees of ptau pathology with similar ptau patterns and AT8 coverage, suggesting that the effect of apoE on tau histopathology is primarily mediated by apoE modulating microglial function.

We next performed biochemical analysis for these samples. Mouse posterior cortical tissue was extracted sequentially in reassembly buffer (RAB; salt buffer), radioimmunoprecipitation assay buffer (RIPA; detergent buffer), and 70% formic acid (FA), which contain soluble, less soluble, and highly insoluble proteins, respectively. Ptau and human tau levels in each fraction were analyzed via quantitative ELISA. We found that PLX3397 treatment significantly reduced ptau levels in both TE4 and TEKO mice (Fig. 5 A). Surprisingly, while comparable human tau levels between groups were observed in most fractions, there was a significant increase of insoluble tau level in PLX3397-treated TE4 mice relative to control TE4 mice, despite preserved brain volume in PLX3397-treated TE4 mice (Fig. 5 B). The elevation of insoluble tau was likely a secondary effect of PLX3397 treatment and appeared to be associated with *Apoe* status, as no difference was observed between control and PLX3397-treated TEKO mice. The concurrence of increased insoluble tau and attenuated brain atrophy suggests that formation of insoluble tau does not directly cause neurodegeneration manifested as brain volume loss.

PLX3397 treatment in TE4 mice induces a marked elevation of soluble apoE present in astrocytes and neurons that positively correlates with ptau and insoluble human tau levels

Based on the protective effect of apoE deficiency on neurodegeneration, we reasoned that PLX3397 treatment may reduce apoE levels in TE4 mice. However, we unexpectedly observed a four to fivefold increase of soluble apoE levels in PLX3397- treatedTE4

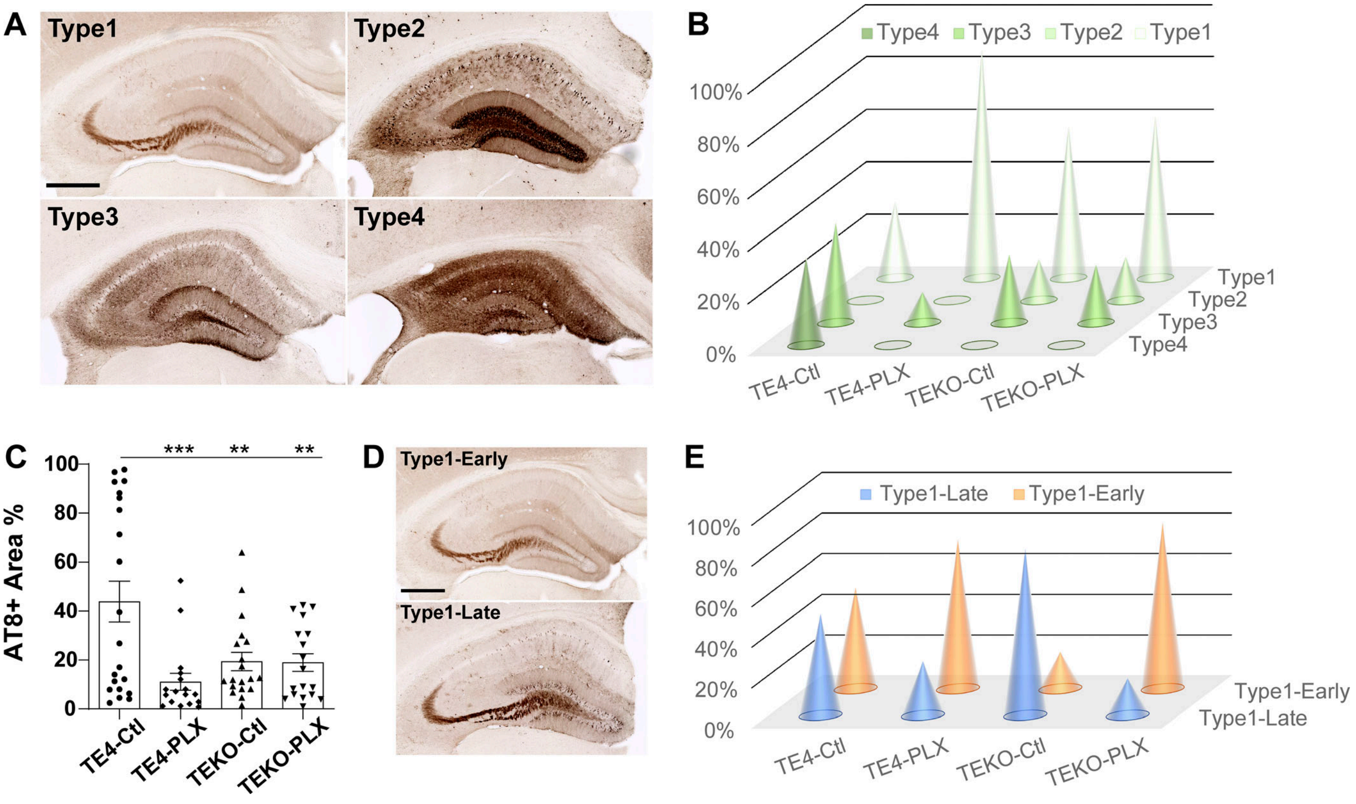

Figure 4. **Microglia drive tau pathogenesis and mediate apoE's effect on tau pathogenesis. (A)** Representative images of the four major ptau staining patterns in 9.5-mo-old TE4 and TEKO mice. Scale bar = 500 µm for all images. **(B)** Distribution of the four ptau staining patterns in 9.5-mo-old TE4 and TEKO mice treated with control (Ctl) or PLX3397-supplemented (PLX) chow (TE4-Ctl: *n* = 21; TE4-PLX: *n* = 17; TEKO-Ctl: *n* = 19; TEKO-PLX: *n* = 18). Fisher's exact test, two-sided (all groups: $P = 2.2 \times 10^4$; TE4-Ctl vs. TE4-PLX: $P = 4.1 \times 10^4$; TE4-Ctl vs. TEKO-Ctl: $P = 4.1 \times 10^4$). **(C)** Quantification of ptau (AT8)-covered area in the hippocampus of these mice. **(D)** Representative images of early-type1 and late-type1 ptau staining patterns within the type1 category (same image used for type1 and type1-early in A and D, respectively). Scale bar = 500 µm for both images. **(E)** Distribution of early-type1 and late-type1 ptau patterns in TE4 and TEKO mice harboring the type1 ptau staining pattern (TE4-Ctl: *n* = 6; TE4-PLX: *n* = 15; TEKO-Ctl: *n* = 11; TEKO-PLX: *n* = 11). Fisher's exact test, two-sided (all groups: $P = 0.0097$; TEKO-Ctl vs. TEKO-PLX: $P = 0.0089$). Data are expressed as means ± SEM. One-way ANOVA with Tukey's post hoc test (two-sided). **, $P < 0.01$; ***, $P < 0.001$. The AT8 staining was performed once.

and E4 mice relative to their control chow-treated counterparts, with TE4-PLX mice showing an even higher level of apoE compared to E4-PLX mice (Fig. 5 C). Because the apoE ELISA assay we used is incompatible with RIPA and FA fractions, we were only able to measure apoE levels in the RAB fraction. To exclude the possibility that we were detecting only a specific pool of apoE by ELISA using the monoclonal apoE antibodies and to assess apoE levels in other fractions, we performed immunoblotting for both the RAB and RIPA fractions using a polyclonal apoE antibody. We confirmed a marked elevation of apoE levels predominantly in the RAB fraction in PLX3397-treated TE4 and E4 mice as compared with control mice (Fig. 5 D), indicating a primarily soluble state of elevated apoE.

To understand where the elevated apoE came from, we co-stained apoE with various cell type markers in brain sections. Compared with control TE4 and E4 mice, there was a strong increase in the intensity of apoE signal that largely co-localized with GFAP⁺ astrocytes in both PLX3397-treated TE4 and E4 mice (Fig. 6, A–F). Diffuse apoE staining was also enhanced (Fig. 6, A–D), and no apoE signal was observed in oligodendrocytes (Fig. 6 G). Intriguingly, in PLX3397-treated TE4 mice, apoE staining was also present in cells of neuronal morphology, the signal of which was particularly strong in the dentate gyrus (Fig. 6, A and H–J), CA3 of the hippocampus, and the piriform/entorhinal cortex (Fig. S4). This type of signal was barely observed in PLX3397-treated E4 mice except weakly in the piriform/entorhinal cortex (Fig. S4, A and B), and was not at all present in control TE4 or E4 mice. This apoE staining pattern was verified by five different monoclonal and polyclonal apoE antibodies (data not shown) and by no apoE staining in PLX3397-treated or control TEKO/EKO mice (Fig. 6 E and Fig. S4, A and B). The apoE⁺ neuronal shaped cells did not co-localize with neuronal nuclei (NeuN), a marker for mature neurons (Fig. 6 I and Fig. S4 D), but partially co-localized with ptau-positive neurons (Fig. 6 J), indicating that they very likely represent a subset of neurons. They may be neuronal precursor cells or immature neurons that have been reported to express CSF1R (Nandi et al., 2012), or they may be CSF1R-expressing mature neurons (Luo et al., 2013) that have switched from being NeuN⁺ to NeuN⁻ via transcriptional reprogramming in response to intracellular apoE buildup (either due to de novo apoE synthesis or apoE uptake and accumulation). The number of apoE⁺ neurons in PLX3397-treated TE4 mice varied across samples and appeared to correlate with the amount of ptau signal in individual samples,

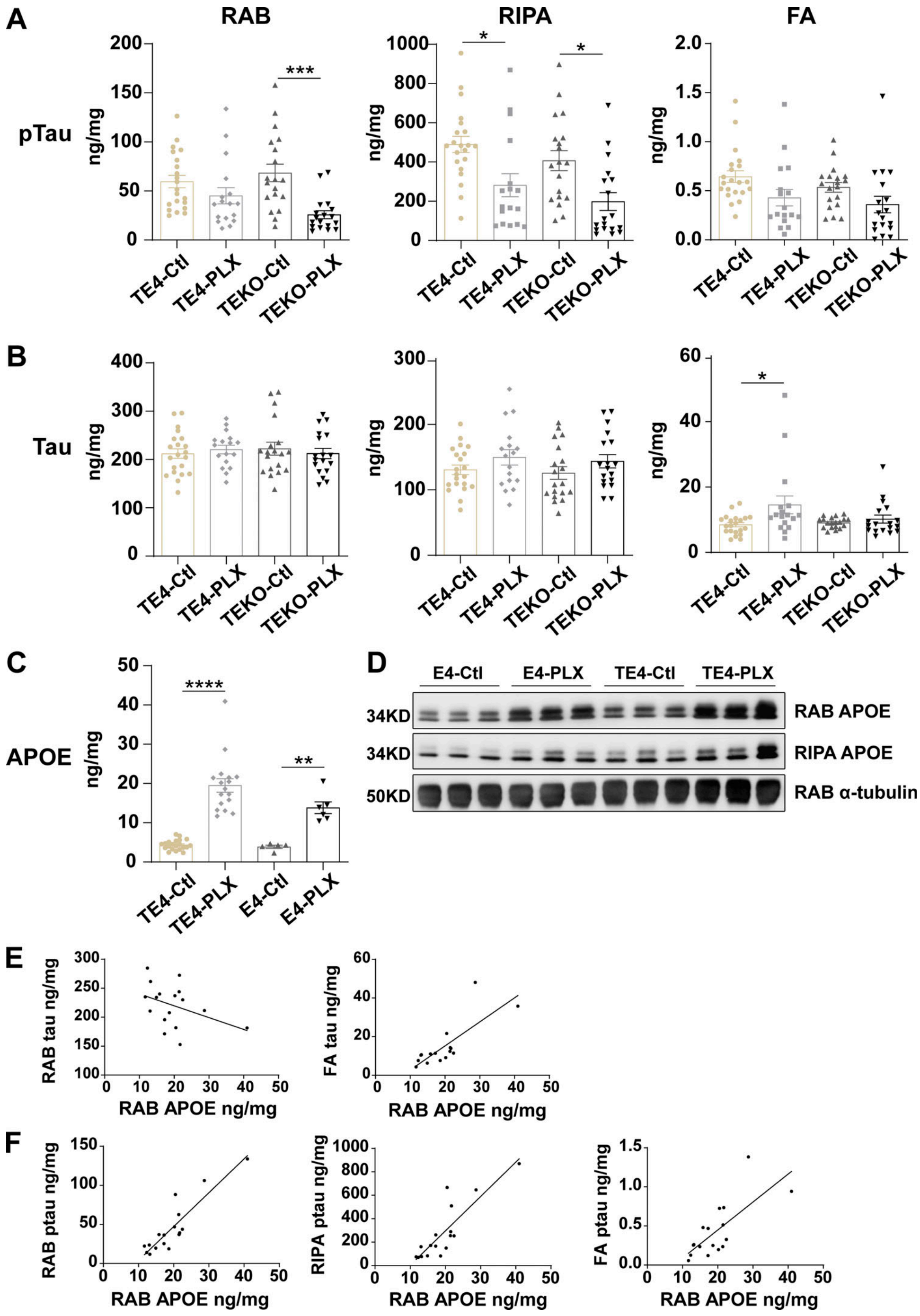

Figure 5. **PLX3397 treatment in TE4 mice results in a sharp elevation of soluble apoE level that correlates with higher ptau and insoluble human tau levels. (A and B)** ELISA results showing concentrations of ptau and human tau in RAB, RIPA, and FA fractions, respectively, for 9.5-mo-old TE4 and TEKO mice treated with control (Ctl) or PLX3397-supplemented (PLX) chow (TE4-Ctl: *n* = 21; TE4-PLX: *n* = 17; TEKO-Ctl: *n* = 19; TEKO-PLX: *n* = 18). **(C)** Human apoE level in the RAB fraction for 9.5-mo-old TE4 and E4 mice treated with control or PLX-supplemented chow (TE4-Ctl: *n* = 21; TE4-PLX: *n* = 17; E4-Ctl: *n* = 12; E4-PLX: *n* = 6). **(D)** Western blot probing for human apoE in the RAB and RIPA fractions for 9.5-mo-old TE4 and E4 mice treated with control or PLX3397-supplemented chow (*n* = 3 per group). **(E)** Correlation of RAB-soluble apoE level with soluble and insoluble human tau levels, respectively. Pearson correlation analysis (two-sided). RAB apoE vs. FA tau: R^2 = 0.6240, P = 0.0002; RAB apoE vs. RAB tau: R^2 = 0.1581, P = 0.1. **(F)** Correlation of RAB-soluble apoE level with ptau levels in the RAB, RIPA, and FA fractions, respectively, in PLX3397-treated TE4 mice. Pearson correlation analysis (two-sided). RAB apoE vs. RAB ptau: R^2 = 0.8039, P < 0.0001; RAB apoE vs. RIPA ptau: R^2 = 0.7312, P < 0.0001; RAB apoE vs. FA ptau: R^2 = 0.5369, P = 0.0008. Data are expressed as means ± SEM. One-way ANOVA with Tukey's post hoc test. *, P < 0.05; **, P < 0.01; ***, P < 0.001; ****, P < 0.0001. All ELISAs were repeated twice.

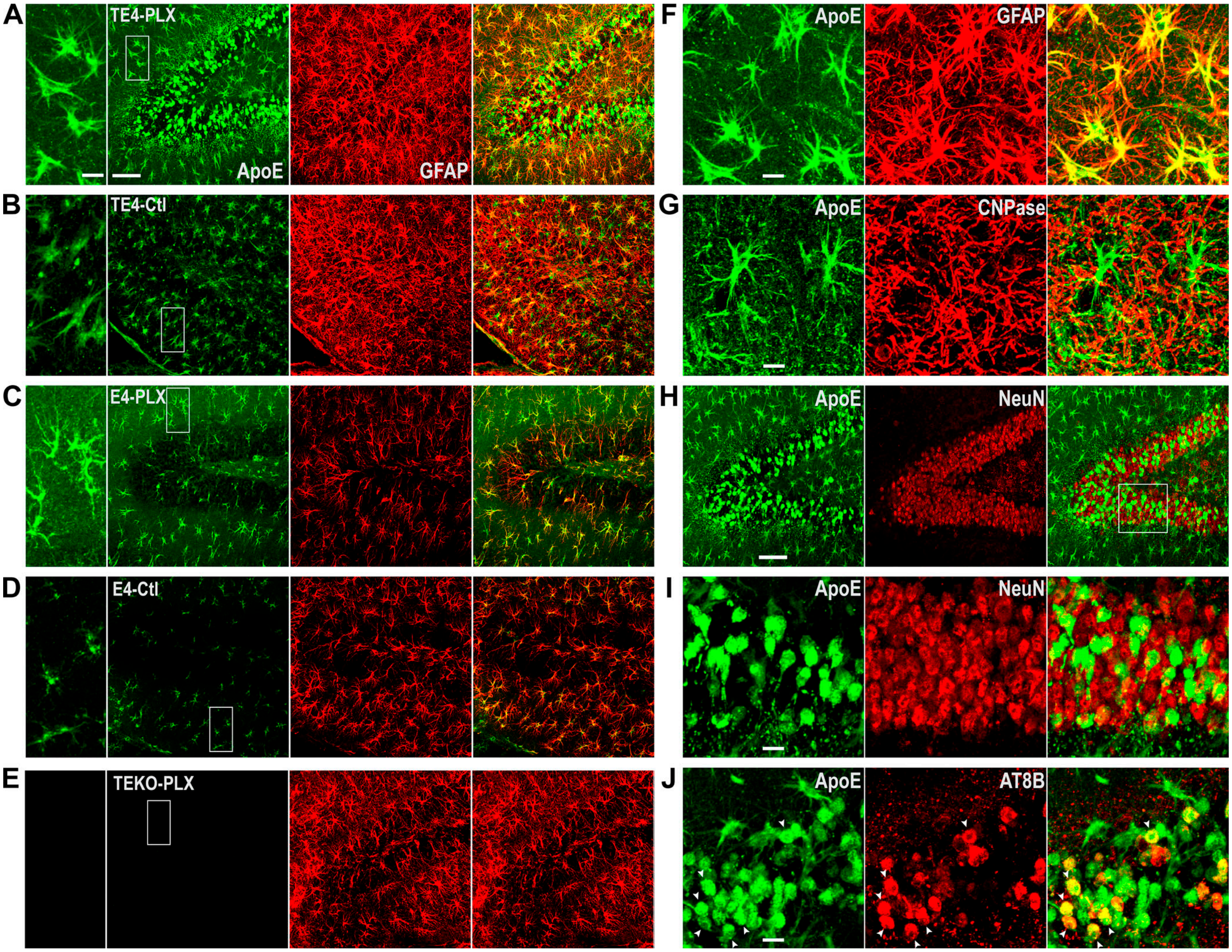

Figure 6. **Elevated apoE in PLX3397-treated TE4 mice is present in astrocytes and a subset of NeuN$^-$ neurons. (A–E)** Representative images of apoE (green, first column), GFAP (red, second column), and merged apoE/GFAP (third column) staining in the hippocampus of 9.5-mo-old TE4-PLX, TE4-Ctl, E4-PLX, E4-Ctl, and TEKO-PLX mice, respectively. Scale bar = 50 µm for all images in the three columns. Far left column: zoom-in of the selected area in respective apoE staining images. Scale bar = 10 µm. **(F)** Co-localization of apoE with GFAP$^+$ astrocytes in TE4-PLX mouse hippocampus. Scale bar = 10 µm. **(G)** Non-co-localization between apoE and CNPase$^+$ oligodendrocytes in TE4-PLX mouse hippocampus. Scale bar = 10 µm. **(H)** Non-co-localization between apoE and NeuN in TE4-PLX mouse dentate gyrus. Scale bar = 50 µm. **(I)** Zoom-in of the selected area in H. Scale bar = 10 µm. **(J)** Partial co-localization of apoE with AT8$^+$ neurons in TE4-PLX mouse dentate gyrus. Arrowheads point to some co-localized neurons. Scale bar = 10 µm. For F–J, the third column is a merged image of the first two columns. ApoE staining was repeated seven times using different antibodies.

suggesting that tau pathology likely increases the sensitivity of these neurons to CSF1R signaling and promotes neuronal apoE buildup upon CSF1R blockage. Overall, while elevated apoE in PLX3397-treated E4 and TE4 mice primarily came from astrocytes, the additional elevation of apoE in TE4-PLX mice over E4-PLX mice appeared to be due to an increased apoE level in subsets of neurons.

Interestingly, we found that the level of RAB-soluble apoE correlated with a lower level of soluble tau and a higher level of insoluble tau in PLX3397-treated TE4 mice (Fig. 5 E). In addition, there was a strong positive correlation between apoE level and ptau levels in all three fractions (Fig. 5 F). These correlations remained significant even after excluding the samples that showed incomplete microglial depletion (data not shown), indicating that apoE derived from astrocytes and likely neurons may directly regulate tau pathogenesis by promoting ptau generation and insoluble tau formation independent of the impact of microglia. However, this direct effect of apoE on tau pathogenesis by itself was insufficient to impact neurodegeneration.

The neuroprotective effect of PLX3397 is unlikely due to its direct impact on neurons

Previous studies report CSF1R expression in small subsets of neurons under normal conditions, and the expression goes up with neuronal injury (Wang et al., 1999; Luo et al., 2013). Therefore, it is possible that PLX3397 protects against neurodegeneration via a direct effect on neurons. However, neuronal CSF1R signaling has been shown to promote neuronal survival (Wang et al., 1999; Nandi et al., 2012; Luo et al., 2013; Chitu et al., 2016). Therefore, assuming PLX3397 indeed affects neuronal

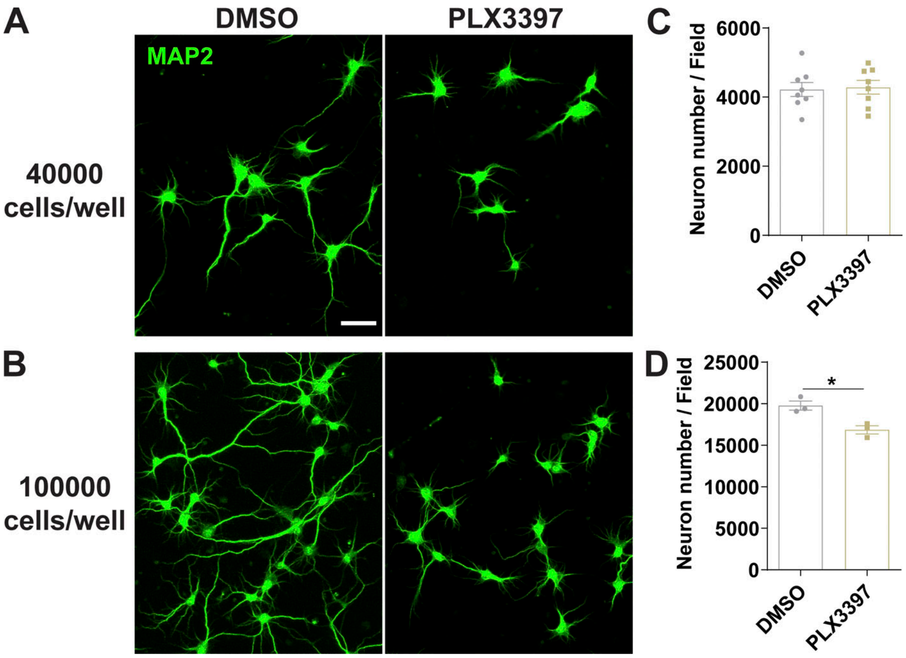

Figure 7. **PLX3397 does not have a direct protective effect on neurons. (A and B)** Primary hippocampal neurons derived from E17 apoE4 KI mouse embryos were infected with AAV2/8-Syn-P301S tau, and cultured at a density of 40,000 or 100,000 cells/well, respectively, in 24-well plates for 8 d in AraC-supplemented medium. The neurons were treated with either DMSO or 8.5 µM PLX3397 at plating. Representative images of neurons stained with MAP2. Scale bar = 50 µm for all images. **(C and D)** Quantification of neuron cell numbers in each imaging field. For 40,000 cells/well: $n = 8$ replicates per group; for 10,000 cells/well: $n = 3$ replicates per group. Data are expressed as means ± SEM. Unpaired two-tailed Student's t test. *, $P < 0.05$. This experiment was performed once.

function, it would be likely to have a detrimental rather than protective effect on neurons.

To understand whether and how PLX3397 might directly impact neurons, we cultured hippocampal neurons derived from apoE4 knockin (KI) mice in cytarabine (AraC)-supplemented medium and infected the neurons with adeno-associated virus (AAV)2/8-Syn-P301S Tau. We treated the neurons with either DMSO or 8.5 µM PLX3397 (comparable to PLX3397 concentration in drug-treated mouse brains) at plating and maintained the culture for 8 d. No astrocytes or microglia were detected by the end of the experiment. At a lower plating density (40,000 cells/well), PLX3397 did not affect neuronal cell number, but mildly inhibited neurite outgrowth (Fig. 7, A and B). At a higher density (100,000 cells/well), the inhibition of neurite outgrowth by PLX3397 became highly prominent, and a mild reduction of neuron number was observed (Fig. 7, C and D). These results were consistent with previous studies showing that CSF1R signaling promotes neuronal survival and neuronal differentiation (Wang et al., 1999; Nandi et al., 2012; Luo et al., 2013; Chitu et al., 2016), suggesting that the neuroprotective effect of PLX3397 in TE4 mice was likely not due to a direct effect of PLX3397 on neurons.

Effects of PLX3397 treatment on blood cell phenotyping

To understand whether PLX3397 affects blood cell populations other than microglia in the brain, we performed complete blood count (CBC) for mouse whole blood as well as flow cytometry for white blood cells in all groups of mice. CBC results showed that PLX3397 treatment significantly reduced the number of RBCs (RBC and hematocrit %) and hemoglobin levels (hemoglobin and mean corpuscular hemoglobin concentration), while increasing the size of RBCs (mean corpuscular volume) in all groups (Fig. 8 A). The number of platelets was also reduced (Fig. 8 B). Interestingly, PLX3397 treatment reduced the total number of white blood cells in E4 and TE4 mice, but not in EKO and TEKO mice (Fig. 8 C), suggesting an apoE-dependent effect on white blood cells under PLX3397 treatment. Detailed analysis by flow cytometry (gating strategy summarized in Fig. S5) revealed that PLX3397 treatment reduced or showed a trend of reducing the frequency of dendritic cells (DCs), natural killer (NK) cells, and Ly6C$^-$ monocytes in all groups of mice (Fig. 8, D–F). PLX3397 preferentially targeted Ly6C$^-$ monocytes over Ly6C$^+$ monocytes, including Ly6C^{hi} and Ly6C^{lo} monocytes (Fig. 8 F). We found that in control chow-treated mice, Ly6C$^+$ monocytes expressed a significantly higher level of CSF1R (CD115) compared with Ly6C$^-$ monocytes (Fig. 8 G), suggesting a higher tolerance to CSF1R inhibition-induced cell death by Ly6C$^+$ monocytes. Interestingly, PLX3397 treatment led to a notable reduction of CSF1R expression in Ly6C$^+$ monocytes and a milder CSF1R reduction in Ly6C$^-$ monocytes, with all surviving monocyte populations expressing a similarly low level of CSF1R (Fig. 8 G). Therefore, while the initial CSF1R expression level may be a key factor determining the susceptibility of monocytes to PLX3397-induced cell death, blockage of CSF1R signaling down-regulated CSF1R expression in the surviving monocytes and converted them to a phenotype that was less dependent on CSF1R signaling. No difference in neutrophil levels was observed between groups, whereas eosinophils showed a trend of increased frequency upon PLX3397 treatment (data not shown). Interestingly, EKO and TEKO mice showed an overall increased frequency of multiple myeloid cell types compared with E4 and TE4 mice, suggesting that apoE deficiency is associated with a higher proliferative capacity of certain myeloid cells. On the other hand, there appeared to be an overall trend of increased T cell frequency (Fig. 8 H) upon PLX3397 treatment. This effect was most pronounced in TEKO mice and was observed in all the T cell subpopulations, including regulatory T cells (T reg cells; Fig. 8 I), CD4$^+$ T cells, CD8$^+$ T cells, memory T cells, and NK T cells (other data not shown). In addition, there was a trend of increased B cell frequency in control TE4 mice over other groups (Fig. 8 J). The significance of these

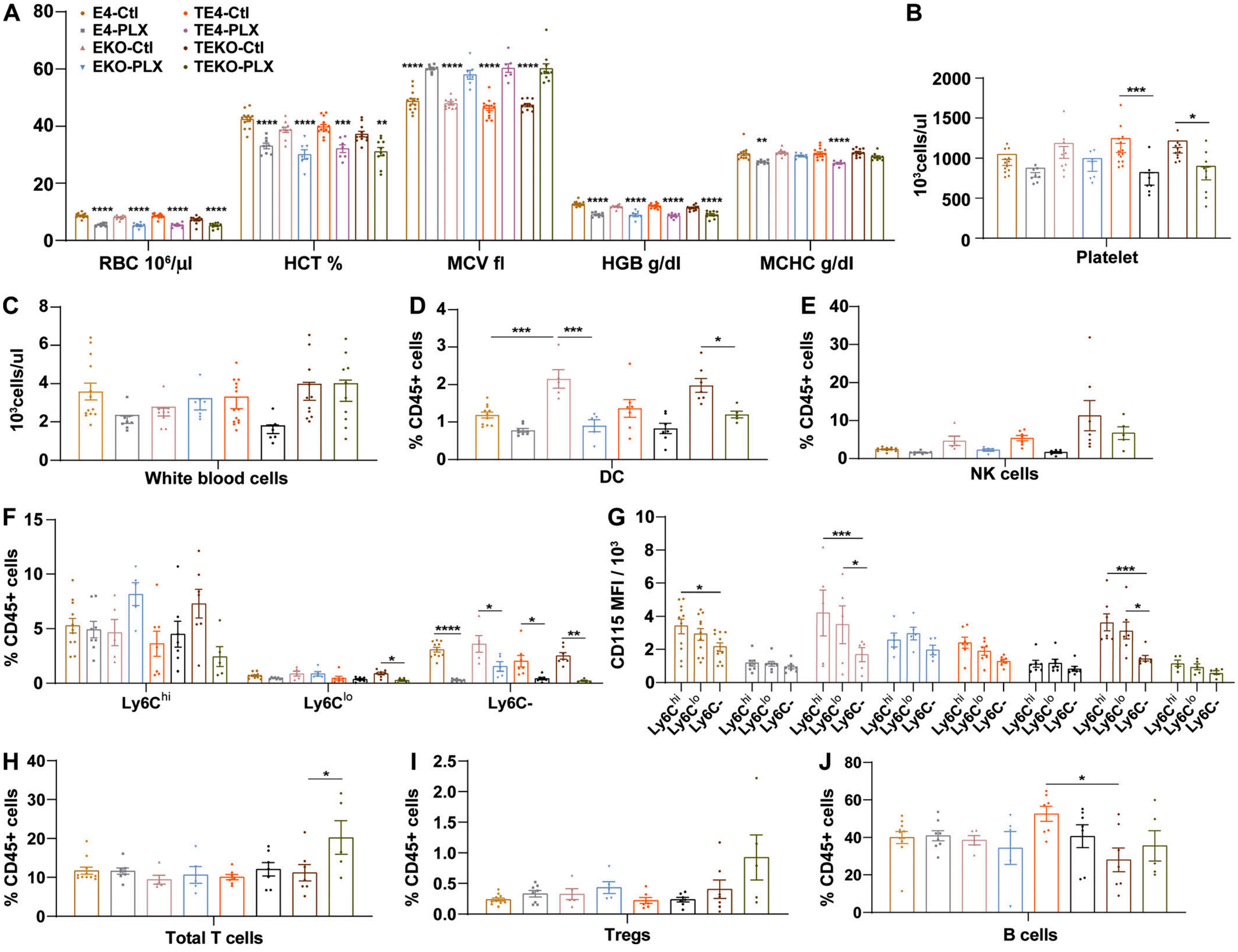

Figure 8. **PLX3397 treatment and apoE status regulate blood cell phenotyping. (A–C)** Complete blood cell count results for the level of RBCs, hemoglobin, platelets, and white blood cells in 9.5-mo-old mice of all genotypes treated with control (Ctl) or PLX3397-supplemented (PLX) chow (TE4-Ctl: *n* = 14; TE4-PLX: *n* = 7; TEKO-Ctl: *n* = 11; TEKO-PLX: *n* = 10; E4-Ctl: *n* = 13; E4-PLX: *n* = 8; EKO-Ctl: *n* = 10; EKO-PLX: *n* = 7). **(D–F)** Flow cytometry quantification of the frequency of DCs, NK cells, Ly6C^{hi}, Ly6C^{lo}, and Ly6C^{-} monocytes, respectively (TE4-Ctl: *n* = 7; TE4-PLX: *n* = 7; TEKO-Ctl: *n* = 7; TEKO-PLX: *n* = 5; E4-Ctl: *n* = 11; E4-PLX: *n* = 8; EKO-Ctl: *n* = 5; EKO-PLX: *n* = 5). **(G)** Median fluorescence intensity (MFI) of CSF1R (CD115) in Ly6C^{hi}, Ly6C^{lo}, and Ly6C^{-} monocytes in all groups of mice (two-way ANOVA with Sidak's post hoc test). **(H–J)** Population frequencies for T cells, T reg cells, and B cells, respectively. Data are expressed as means ± SEM. One-way ANOVA with Tukey's post hoc test. *, $P < 0.05$; **, $P < 0.01$; ***, $P < 0.001$; ****, $P < 0.0001$. HCT, hematocrit; HGB, hemoglobin; MCHC, mean corpuscular hemoglobin concentration; MCV, mean corpuscular volume . The CBC and flow cytometry experiments for blood cell phenotyping were performed >10 times.

blood cell changes and their potential influence on brain pathogenesis and neurodegeneration are still unclear, and need to be further addressed in future studies.

Discussion

AD and many other neurodegenerative diseases are known as proteopathies characterized by accumulation of misfolded and aggregated proteins. For decades, research and drug development in the AD field have largely focused on the two pathological protein hallmarks of AD, amyloid-β and tau pathology. Given a high correlation between tau pathology and AD clinical readouts (Arriagada et al., 1992; Josephs et al., 2008), pathological tau-induced cell-autonomous neurotoxicity was believed to play a key role in driving neurodegeneration. It was not until recently that the role of brain innate immunity in AD and tauopathy pathogenesis became increasingly recognized. While it is widely acknowledged that chronic innate immune activation in the brain can cause neuronal loss, the interaction between innate immunity and tau pathology and their respective contributions to neurodegeneration are not well understood. This is largely due to an intertwined relationship between tau pathogenesis and innate immunity, making it difficult to separate the two effects. With complete microglial depletion, we were able to assess the impact of microglia on tau pathogenesis, as well as the effect of tau pathology on neurodegeneration, independent of the influence of microglia-mediated inflammation on neurodegeneration.

Here, we demonstrated that microglia served as the driving force of neurodegeneration in a mouse model of tauopathy.

Depletion of microglia in TE4 mice upon neurodegeneration onset fully blocked development of brain atrophy. Importantly, in the absence of microglia, progression of ptau pathology was halted, indicating that ptau pathogenesis is also predominantly driven by microglia-mediated inflammation. It is unclear whether the rescue of neurodegeneration in the absence of microglia resulted from a direct attenuation of inflammation-induced neuronal loss or was an indirect result of blocked ptau pathology due to lack of tau-induced neurotoxicity. While we cannot exclude the role of tau pathology in inducing neurodegeneration, our results suggest that ptau pathology progresses very slowly in the absence of microglia. Whether tau pathology could progress to an advanced stage within a normal lifespan independent of microglia to affect neurodegeneration is uncertain. In addition, PLX3397-treated TE4 mice showed a preserved brain volume despite harboring an increased level of insoluble tau compared with control TE4 mice, suggesting that certain forms of pathological tau do not directly cause neuronal death. This is consistent with previous reports that tau tangles are off the pathway of acute neuronal death (de Calignon et al., 2009, 2010; Kuchibhotla et al., 2014). Therefore, microglial activation, rather than pathological tau-induced neurotoxicity, is likely the key factor dictating disease progression in this model. We did not observe a difference of GFAP immunoreactivity between PLX3397-treated and control groups, suggesting that GFAP$^+$ astrocytes do not directly regulate neurodegeneration. However, it is possible that astrocytes crosstalk with microglia to influence neurodegeneration. Regardless, the fact that microglial depletion is sufficient to block tau pathology and neurodegeneration suggests that microglia play a key role in mediating neurodegeneration.

Interestingly, a previous study showed that a mild microglia reduction (~30%) by PLX3397 treatment did not change tau burden or cortical atrophy in a tauopathy mouse model (Bennett et al., 2018). We found that the retention of even a small population of activated microglia was associated with more neurodegeneration compared with complete microglial eradication, suggesting a potent role of activated microglia in regulating neurodegeneration and the requirement of depletion of the vast majority of microglia in order to reveal their effects on neurodegeneration. We surprisingly found a mouse chow- and sex-dependent effect on the efficiency of microglial depletion, revealing the complexity of immune regulation that can be easily neglected. While the effects appeared to be due to differences in plasma PLX3397 levels, whether plasma PLX3397 concentration is affected by food digestion/absorption, drug catabolism regulated by blood cell composition that is potentially affected by chow type or sex, or other factors is unknown. We found that the chow formulas indeed could affect blood cell phenotypes. For instance, Purina 5053 resulted in an increase of the neutrophil population and a concomitant down-regulation of the lymphocyte population compared with AIN-76A (data not shown). These variables should be taken into consideration in future studies.

We identified a critical difference between microglial proliferation and microglial activation, the concepts of which have not always been clear in previous studies. Control TEKO mice showed no difference and even a trend of higher level of Iba1$^+$ microglia compared with control TE4 mice, despite a marked rescue of brain volume loss in TEKO mice. In contrast, the level of CD68$^+$-activated microglia was notably lower in control TEKO mice and highly correlated with the level of neurodegeneration, suggesting that the activation status of microglia, rather than the absolute number of microglia, is functionally associated with neurodegeneration. Microglial proliferation represents one aspect of microglial biology upon stimulation, but is not necessarily linked with transcriptional programming that converts microglia to an activated neurodegenerative phenotype. ApoE deficiency does not block the proliferating capacity of microglia. In fact, it appears to increase microglial numbers under certain stimulating conditions, such as mild neurodegeneration as was observed in control TEKO mice, or LPS stimulation as was reported in previous literature (Zhu et al., 2012). We also observed a larger population of certain blood myeloid cells in EKO and TEKO mice relative to TE4 and E4 mice. In addition, TEKO and EKO mice presented a higher resistance to PLX3397-induced microglial cell death relative to TE4 and E4 mice, with preservation of predominantly nonactivated microglia. This evidence suggests that apoE deficiency promotes the proliferation and survival of certain myeloid cell lineages but may interfere with their functional maturation. In the brain, apoE deficiency prevents microglia from acquiring an activated status featuring a neurodegenerative phenotype that promotes neural injury (Krasemann et al., 2017). How apoE controls the survival, proliferation, and activation of microglia is unclear. One possibility is through regulating CSF1R signaling. However, detailed studies are needed in the future to address this question.

We previously uncovered a significant role of apoE in regulating neurodegeneration in the setting of tauopathy. We proposed two major mechanisms through which apoE modulates neurodegeneration: 1) apoE regulates tau pathogenesis (i.e., progression of ptau stages); and 2) apoE regulates glia-mediated innate immunity. However, the respective contribution of the two mechanisms to apoE's effect on neurodegeneration was unclear, given that the effect of apoE on tau pathogenesis was obscured by effects of apoE on innate immunity. Our current experimental scheme allows simultaneous assessment of the two aspects. We found that the effect of apoE on neurodegeneration was eliminated in the absence of microglia, suggesting a central role of microglia in mediating apoE's effect on neurodegeneration. Importantly, effects of apoE on ptau stage progression and ptau immunoreactivity were also abolished upon microglial depletion, suggesting that the effect of apoE on tau pathogenesis was primarily driven by the effect of apoE on microglial function, and there was no direct effect of apoE on tau histopathology in the absence of microglia. This supports the notion that the effect of apoE on neurodegeneration in the tauopathy model predominantly results from apoE regulating microglial function.

It is possible that the lack of apoE's effect on tau pathology in PLX3397-treated TE4 and TEKO mice was complicated by the significantly higher level of retained microglia in TEKO mice relative to TE4 mice. These excessive microglia in TEKO mice, although mostly being CD68$^-$ that were not associated with neuronal loss, may still be able to affect tau pathogenesis, for instance, by producing factors to induce tau phosphorylation.

To assess the effect of apoE on tau pathogenesis completely independent of the impact of microglia, we analyzed the level of apoE, tau, and ptau only in PLX3397-treated TE4 mice that showed complete elimination of microglia. Interestingly, we found a significant positive correlation of salt-soluble brain apoE levels with both ptau and insoluble tau levels in these mice, suggesting a potential direct role of apoE present in astrocytes and neurons in promoting ptau and insoluble tau formation. However, this effect of apoE on pathological tau generation did not contribute to brain volume loss and therefore did not significantly account for apoE's effect on neurodegeneration.

Our previous finding that apoE deficiency strongly protects against neurodegeneration suggests that lowering apoE levels may be beneficial. Here, we surprisingly found a marked elevation of apoE in both astrocytes and neurons in TE4 mice upon PLX3397 treatment. The elevated apoE level in PLX3397-treated TE4 mice may be related to the higher insoluble tau level in these mice, given the correlation between apoE and insoluble tau levels. However, in contrast to control TE4 mice that showed severe neurodegeneration, PLX3397-treated TE4 mice showed full rescue of brain volume despite a higher apoE level. This result illustrates a critical concept that the absolute amount of apoE is not the only key to neurodegeneration. The effect of apoE on neurodegeneration is dependent on the presence of microglia. How does apoE function through microglia to induce neurodegeneration? On the one hand, microglia-derived apoE cell-autonomously regulates the acquisition of the neurodegenerative phenotype by microglia that leads to neural injury. It is possible that the source and location of apoE, in addition to the quantity of apoE, matter for neurodegeneration. ApoE present in astrocytes and neurons may regulate ptau and insoluble tau formation that is not associated with acute neuronal loss; whereas microglia-derived apoE controls neurodegenerative microglial activation and functions, and therefore may be essential for neurodegeneration. On the other hand, apoE may serve as an opsonin coating the surface of injured or dead neurons, and recruit activated microglia via an apoE–TREM2 interaction to promote neuronal phagoptosis by microglia (Shi and Holtzman, 2018), therefore exacerbating neurodegeneration.

Neuroinflammation in AD is primarily driven by microglia and astrocytes. However, it's likely that blood-circulating immune cells crosstalk with central nervous system glia cells, for instance, via cytokine exchange, to influence disease pathogenesis. Emerging evidence that gut microbiota regulate microglial maturation and function (Erny et al., 2015; Thion et al., 2018) supports this possibility. Previous literature reported inconsistent results regarding the effect of PLX3397 on blood monocytes (Chitu et al., 2012; Sluijter et al., 2014), and detailed studies of PLX3397's impact on other blood cell types are rare. Here, we performed blood cell phenotyping for a full panel of major blood cell types to assess the effect of PLX3397 treatment, apoE genotype, and disease status on blood cell composition. We found that at a dose of 400 mg/kg chow, PLX3397 treatment had a significant impact on the myeloid-megakaryocyte-erythroid cell lineages, leading to a reduction of RBCs, platelets, DCs, and Ly6C$^-$ monocytes. NK cells showed a similar reduction despite being a lymphoid lineage. The enlarged cell body of erythrocytes indicates a slowing of DNA synthesis that prevents normal cell division (Hesdorffer and Longo, 2015). This suggests that PLX3397 may prohibit the proliferation of committed precursors of the affected cells. Granulocytes showed either an opposite pattern or no change, suggesting a relatively independent or compensatory regulation mechanism. Corresponding to an overall reduction of myeloid cells, PLX3397 increased the frequency of T cells, particularly in TEKO mice. The effect of apoE on blood cell phenotyping was mainly reflected in increased myeloid cell populations in apoE-deficient mice, which was in line with a higher cell proliferation capacity associated with apoE deficiency. Interestingly, B cell frequency was uniquely elevated in control TE4 mice over other groups, suggesting a potential link between B cell function and neurodegeneration. However, the meaning of these blood cell changes and whether they are functionally connected to microglia in the brain requires further investigation.

In summary, we demonstrated that microglial activation, rather than tau-induced direct neurotoxicity, is the driving force of neurodegeneration in the setting of tauopathy. Critically, the progression of ptau pathology by itself is driven by microglia. In addition, microglia are the key mediator of apoE's effect on neurodegeneration. Therefore, therapeutic strategies targeting microglia may be a highly effective approach to prevent disease progression. A deeper understanding of the neurodegenerative microglial signature and how to specifically engineer and control microglial functions may be a key to the design and development of microglia-targeted therapies.

Materials and methods

Animals

P301S tau transgenic mice (#008169; The Jackson Laboratory) expressing human P301S 1N4R tau driven by the PrP promoter were backcrossed and maintained on a C57BL/6 background. Human *APOE4* KI mice (C57BL/6) were provided by P.M. Sullivan, and *Apoe* KO mice (C57BL/6) were purchased from The Jackson Laboratory (#002052). P301S mice were crossed to *APOE4* KI or *Apoe* KO mice to generate TE4 and TEKO mice, respectively. All animal procedures and experiments were performed under guidelines approved by the animal studies committee at Washington University School of Medicine.

PLX3397 formulation in mouse chow.

PLX3397 was provided by Plexxikon Inc. For the initial chow characterization study, PLX3397 was formulated in either the Purina 5053 (Lab Supply) chow or the AIN-76A (Research Diets) chow at a concentration of 300 mg/kg chow. For the formal study, PLX3397 was formulated in the AIN-76A (Research Diets) chow at a concentration of 400 mg/kg chow.

PLX3397-supplemented chow characterization

Mice were fed with either AIN-76A or Purina 5053 chow supplemented with 300 mg/kg PLX3397 for 7 d. The amount of chow consumption for each mouse was measured every 24 h over the 7-d period, and was normalized to mouse weight to obtain the amount of chow consumption per gram of mouse weight each day. This value was further converted to the amount of drug consumption per day per gram of mouse weight by multiplying the drug concentration and the drug incorporation rate in diet. Plasma drug concentrations and drug incorporation rate in diet were measured by Integrated Analytical Solutions, Inc., via liquid chromatography tandem-mass spectrometry.

Brain section staining

For AT8 histological staining, frozen brain sections were washed three times in Tris-buffered saline (TBS) buffer followed by incubation in 0.3% hydrogen peroxide in TBS for 10 min. Sections were then washed and blocked with 3% milk in 0.25% TBS-X (Triton X-100) for 0.5 h, followed by incubation at 4°C overnight with biotinylated AT8 antibody (MN1020B; Thermo Fisher Scientific). The next day, the slices were developed using the VECTASTAIN Elite ABC HRP Kit (Vector Laboratories) following the manufacturer's instructions. Stained sections were imaged by the NanoZoomer digital pathology system, and pathology was quantified using Image J. For immunofluorescence staining, sections were washed in TBS three times and blocked in blocking buffer (3% BSA + 3% goat serum in 0.3% TBS-X) for 0.5 h at room temperature (RT), followed by overnight incubation at 4°C with primary antibodies in stain buffer (1% BSA + 1% goat serum in 0.3% TBS-X). ApoE and 2′,3′-cyclic nucleotide 3′-phosphodiesterase (CNPase) staining required antigen retrieval in sodium citrate buffer (10 mM sodium citrate, 0.05% Tween 20, pH 6.0) at 95°C for 30 min before blocking. The next day, the sections were washed in TBS and incubated with fluorescence-labeled secondary antibodies (Molecular Probes) for 1 h at RT. The slices were then washed and mounted in Prolong Gold antifade mounting media (P36931; Molecular Probes). Images for Iba1, CD68, and GFAP staining in Fig. 2, Fig. 3, and Fig. S3 were taken using the Cytation 5 imager at 4× magnification with image stitching and quantified using Image J. Images for apoE colocalization experiments were taken with a Nikon A1Rsi Confocal Microscope at 40× magnification. Images for Iba1 staining in the chow characterization experiments were taken by an epifluorescence microscope at 4× or 10× magnification and quantified using MetaMorph. Primary antibodies were as follows: CD68 (MCA1957, 1:500; AbD SeroTec), GFAP (MAB3402, 1:2,000; EMD Millipore), Iba1 (019–19741, 1:5,000; Wako), ApoE (13366S, 1:500; Cell Signaling), CNPase (836404, 1:500; BioLegend), and NeuN (MAB377, 1:100; EMD Millipore).

Volumetric analysis

Brain volume was quantified as described (Shi et al., 2017). Briefly, the left hemisphere of brain was sectioned coronally at 50 µm, and every sixth coronal brain section (300 µm between sections) starting rostrally at bregma +2.1 mm to the dorsal end of the hippocampus at bregma −3.9 mm was mounted for each mouse. All mounted sections were stained with 0.1% Sudan black in 70% ethanol at RT for 20 min and then washed in 70% ethanol. The sections were finally washed in Milli-Q water and coverslipped with Fluoromount. The stained slices were imaged with the NanoZoomer, and areas of interest were traced and measured in each slice using the NanoZoomer Digital Pathology viewer. The volume was calculated using the following formula: volume = (sum of area) × 0.3 mm. For hippocampus and posterior lateral ventricle, quantification started from bregma −1.1 and ended at bregma −3.9. For piriform/entorhinal cortex, quantification started at bregma −2.3 and ended at bregma −3.9.

Brain extraction

Mouse posterior cortical tissue was processed in RAB, RIPA, and 70% FA buffer sequentially. The tissue was first weighed and homogenized using an electric pestle at 10 µl buffer/1 mg tissue in RAB buffer (100 mM 2-(N-morpholino) ethanesulfonic acid, 1 mM EGTA, 0.5 mM MgSO4, 750 mM NaCl, 20 mM NaF, 1 mM Na_3VO_4, pH 7.0, supplemented by protease inhibitors [Complete; Roche] and phosphatase inhibitors [PhosSTOP; Roche]). After centrifugation at 50,000 ×*g* for 20 min, the supernatant was taken as the RAB-soluble fraction, and the pellet was dissolved in RIPA buffer (150 mM NaCl, 50 mM Tris, 0.5% deoxycholic acid, 1% Triton X-100, 0.1% SDS, 5 mM EDTA, 20 mM NaF, 1 mM Na_3VO_4, pH 8.0, supplemented by Complete and PhosSTOP) at 10 µl buffer/1 mg tissue by sonication at a 30% amplitude for 1 min. After centrifugation at 50,000 ×*g* for 20 min, the supernatant was taken as the RIPA-soluble fraction. The pellet was sonicated in 70% FA at 10 µl buffer/1 mg tissue using the same sonicating parameter, and centrifuged at 50,000 ×*g* for 20 min. The supernatant was taken as the FA-soluble fraction. All fractions were stored in −80°C until analyzed.

ELISA

The ELISA plates were coated with 20-µg/ml coating antibody overnight at 4°C. The next day, the plates were washed in PBS for five times, and mouse brain lysates were diluted in sample buffer (human tau and ptau sample buffer: 0.25% BSA in PBS with 300 µM Tris, pH 7.4; human apoE sample buffer: 0.5% BSA in 0.025% PBS-Tween 20 [PBST]; both buffers were supplemented with protease inhibitors) and loaded into the plates in duplicates. The plates were incubated at 4°C overnight. On the third day, the plates were washed in PBS, followed by addition of the detection antibody and incubation at 37°C for 90 min. The plates were then washed with PBS and incubated with streptavidin-poly-horseradish peroxidase-40 for 90 min at RT. Plates were then washed and developed with Super Slow ELISA 3,3′,5,5′-Tetramethylbenzidine (Sigma) and read at 650 nm. For FA fractions, samples were neutralized with 3 M Tris buffer (pH 8.0) before loading into the plate. Tau5 (gift from L. Binder, Northwestern University, Chicago, IL), HJ14.5 (in house anti-ptau antibody) and HJ15.6 (in house anti-human apoE antibody) were used as coating antibodies, and biotinylated HT7 (MN1000B; Thermo Fisher Scientific), biotinylated AT8 (MN1020B; Thermo Fisher Scientific), and biotinylated HJ15.4 (in house anti-human apoE antibody) were used as detection antibodies for human tau, ptau, and human apoE ELISAs, respectively.

Western blot

Samples from the RAB and RIPA fractions of mouse brain lysates were run for Western blot using 4–12% NuPAGE (Invitrogen) gels in 3-(N-morpholino) propanesulfonic acid buffer and transferred to nitrocellulose membranes. The membranes were blocked with 5% milk in 0.125% PBS-X for 30 min at RT, followed by incubation of primary antibodies (human apoE [ab24139; Abcam] and α-tubulin [T5168; Sigma] overnight at 4°C. The membranes were then washed with 0.0125% PBS-X and incubated with HRP-conjugated secondary antibodies (Santa Cruz) for 1.5 h at RT. Membranes were then washed and developed using the ChemiDoc MP Imaging System (Bio-Rad).

Primary neuron culture and PLX3397 treatment

Primary hippocampal neurons were obtained from E17 apoE4 KI mouse fetuses. Hippocampi were dissected in calcium- and magnesium-free HBSS with careful stripping of meninges. Tissue was digested in HBSS containing 0.25% trypsin (#15090-046; GIBCO) and 0.3 mg/ml DNase (#DN-25; Sigma) at 37°C for 10 min, and was dissociated in HBSS containing 0.4 mg/ml DNase using a fire-polished Pasteur glass pipette and filtered through a 70-µm nylon mesh. Filtered material was pelleted at 1000 ×*g* for 5 min, washed with neurobasal medium (Neurobasal + 1× B27 + 1× penicillin/streptomycin + 1× L-glutamine) once, and infected with AAV2/8-synapsin-P301S tau virus for 3 h on ice. Cells were then pelleted, washed, and plated at a density of 40,000 cells/well or 100,000 cells/well in 500 µl neurobasal medium onto 24-well tissue culture plates that had been coated with 10 µg/ml poly-L-lysine (#P2636; Sigma). At plating, 1 µM AraC was added and replenished at day in vitro 5 to prevent glia growth. The neurons were treated with 8.5 µM PLX3397 (dissolved in DMSO) or DMSO at plating and maintained for 8 d. 200 µl fresh medium containing 8.5 µM PLX3397 or DMSO was supplemented at day in vitro 5.

Immunocytochemistry

At DIV8, neurons were fixed in Dulbecco's PBS containing 4% paraformaldehyde and 4% sucrose at RT for 10 min and permeabilized with 0.3% PBST for 10 min. After blocking in 0.1% PBS-X containing 3% BSA and 3% goat serum for 30 min at RT, cells were incubated with primary antibodies in stain buffer (1% BSA + 1% goat serum in 0.1% PBS-X) overnight at 4°C. The next day, cells were washed three times with 0.1% PBST and incubated in secondary antibodies for 1 h at RT. Cells were then washed three times in 0.1% PBST and mounted in Prolong Gold antifade mounting media (P36931; Molecular Probes). Images were taken using the Cytation 5 imager at 4× magnification using a scheme covering ∼70% of the total area of a well with image stitching for quantification. Representative images were taken at 10× magnification. Image J was used for quantification of neuron number. Primary antibodies were as follows: MAP2 (AB5543, 1:4,000; EMD Millipore), GFAP (MAB3402, 1:2,000; EMD Millipore), ALDH1L1 (ab190298, 1:400; Abcam), and Iba1 (019–19741, 1:5,000; Wako).

Blood cell phenotyping

Mouse blood was collected via cardiac puncture from anaesthetized mice into heparin-rinsed tubes. 60 µl of the whole blood of each animal was immediately sent to Washington University Division of Comparative Medicine Research Animal Diagnostic Laboratory for CBC in a double-blinded manner. The rest of the blood was first subjected to RBC lysis using the Pharm Lyse buffer (555899; BD Biosciences) following the manufacturer's instructions. The remaining white blood cells were washed with PBS and stained with a fixable live/dead cell staining dye (L23102; Thermo Fisher Scientific) on ice for 30 min. The cells were then spun down and washed twice with stain buffer (554656; BD Biosciences), followed by incubation in stain buffer supplemented with mouse Fcγ receptor block reagent (553141; BD Biosciences) on ice for 15 min. A master mix of all the fluorescently tagged antibodies for cell surface markers was created by diluting the antibodies in the FcγR block–containing stain buffer supplemented with the brilliant stain buffer (563794; BD Biosciences). The master mix was then equally distributed to each individual blood sample. The cells were stained on ice for 30 min. After incubation, the cells were washed twice with stain buffer and fixed in the cytofix buffer (554655; BD Biosciences) on ice for 10 min. After fixation, the cells were spun down, resuspended in stain buffer, and run through flow cytometry using a BD LSRFortessa X-20 cell analyzer. The AbC Anti-Rat/Hamster Bead Kit (A10389; Thermo Fisher Scientific), AbC Anti-Mouse Bead Kit (A10344; Thermo Fisher Scientific), and ArC Amine Reactive Compensation Bead Kit (A10346; Thermo Fisher Scientific) were used for setting flow cytometry compensation. Each channel was assigned a fluorescence minus one control to set the threshold for the positive population. Around 90% of samples were collected of 50,000 cells in the $CD45^+$ gate, and the remaining 10% of samples were collected of 100,000 cells in the $CD45^+$ gate. Data analysis and figure generation were performed using FlowJo v10. Antibodies used for flow cytometry are as follows: BUV395 rat anti-mouse CD45 (clone 30-F11, #564279; BD Biosciences), APC-Cy7 rat anti-CD11b (clone M1/70, #557657; BD Biosciences), BV605 hamster anti-mouse CD11c (clone N418, #744179; BD Biosciences), BV650 rat anti-mouse I-A/I-E (clone M5/114.15.2, #563415; BD Biosciences), BV786 rat anti-mouse Siglec-F (clone E50-2440, #740956; BD Biosciences), Alexa Fluor 700 rat anti-mouse Ly-6G (clone 1A8, #561236; BD Biosciences), PerCP-Cy5.5 rat anti-mouse Ly-6C (clone AL-21, #560525; BD Biosciences), BV711 rat anti-mouse CD19 (clone 1D3, #563157; BD Biosciences), Alexa Fluor 647 rat anti-mouse CD25 (clone 7D4, #563598; BD Biosciences), BUV737 rat anti-mouse CD3 Molecular Complex (clone 17A2, #564380; BD Biosciences), PE-Cy7 rat anti-mouse CD4 (clone RM4-5, #552775; BD Biosciences), FITC rat anti-mouse CD8a (clone 53-6.7, #553030; BD Biosciences), PE mouse anti-mouse NK-1.1 (clone PK136, #557391; BD Biosciences), Super Bright 436 rat anti-mouse CD115 (c-fms, clone AFS98; eBioscience, #62-1152-82; Invitrogen), and PE-Cy5 rat anti-mouse CD44 (clone IM7, #553135; BD Biosciences).

Statistical analysis

Unless explicitly stated, all data were shown as means ± SEM. Differences between groups were evaluated by one-way ANOVA tests with post hoc Tukey's multiple comparisons tests. GraphPad Prism version 8 for Windows (GraphPad Software) was used for these analyses and creation of the plots. For statistical analysis of the ptau staining pattern distribution, two-sided Fisher's exact tests were performed using the "fisher.test" function in R version 3.5.2 (The R Foundation for Statistical Computing).

Online supplemental material

Fig. S1 shows that microglial depletion efficiency is affected by both sex and chow formula and correlates with plasma drug concentration. Fig. S2 shows high efficiency of microglial depletion by PLX3397 supplemented in the AIN-76A chow at a 400-mg/kg dose. Fig. S3 shows no difference of GFAP$^+$ astrocytes in PLX3397-treated or control TE4 and TEKO mice, or in their non-tau transgenic counterparts. Fig. S4 shows elevated apoE in astrocytes and NeuN$^-$ neurons in the piriform/entorhinal cortex of PLX3397-treated TE4 and E4 mice compared with control TE4 and E4 mice. Fig. S5 shows the gating strategy for isolating different blood cell types in flow cytometry.

Acknowledgments

We thank Plexxikon Inc. for providing PLX3397 for the study. We thank Andrey Rymar for all the PLX3397-related assistance in the study. We thank Washington University Division of Comparative Medicine Research Animal Diagnostic Laboratory for performing the CBC for the samples.

This study was supported by the National Institutes of Health (NS090934 and AG047644 [to D.M. Holtzman]), the JPB Foundation (to D.M. Holtzman), and the Cure Alzheimer's Fund (to D.M. Holtzman). Experiments were performed in part through the use of Washington University Center for Cellular Imaging supported by Washington University School of Medicine, the Children's Discovery Institute of Washington University, and St. Louis Children's Hospital (CDI-CORE-2015-505) and the Foundation for Barnes-Jewish Hospital (3770).

D.M. Holtzman is listed as inventor on a patent licensed by Washington University to C2N Diagnostics on the therapeutic use of anti-tau antibodies. D.M. Holtzman co-founded and is on the scientific advisory board of C2N Diagnostics, LLC. C2N Diagnostics, LLC has licensed certain anti-tau antibodies to AbbVie for therapeutic development. D.M. Holtzman is on the scientific advisory board of Denali and consults for Genentech and Idorsia. The remaining authors declare no competing financial interests.

Author contributions: Y. Shi conceived the study and designed the experiments. Y. Shi performed the experiments with the help of M. Manis, J. Long, K. Wang, J. Remolina Serrano, and R. Hoyle. P.M. Sullivan provided the human APOE4 KI mice. Y. Shi analyzed the data. Y. Shi and D.M. Holtzman wrote the paper. All authors reviewed and approved the manuscript.

Submitted: 2 June 2019
Revised: 21 July 2019
Accepted: 8 August 2019

References

Arriagada, P.V., J.H. Growdon, E.T. Hedley-Whyte, and B.T. Hyman. 1992. Neurofibrillary tangles but not senile plaques parallel duration and severity of Alzheimer's disease. *Neurology.* 42:631–639. https://doi.org/10.1212/WNL.42.3.631

Bennett, R.E., A. Bryant, M. Hu, A.B. Robbins, S.C. Hopp, and B.T. Hyman. 2018. Partial reduction of microglia does not affect tau pathology in aged mice. *J. Neuroinflammation.* 15:311. https://doi.org/10.1186/s12974-018-1348-5

Chitu, V., V. Nacu, J.F. Charles, W.M. Henne, H.T. McMahon, S. Nandi, H. Ketchum, R. Harris, M.C. Nakamura, and E.R. Stanley. 2012. PSTPIP2 deficiency in mice causes osteopenia and increased differentiation of multipotent myeloid precursors into osteoclasts. *Blood.* 120:3126–3135. https://doi.org/10.1182/blood-2012-04-425595

Chitu, V., Ş. Gokhan, S. Nandi, M.F. Mehler, and E.R. Stanley. 2016. Emerging roles for CSF-1 receptor and its ligands in the nervous system. *Trends Neurosci.* 39:378–393. https://doi.org/10.1016/j.tins.2016.03.005

de Calignon, A., T.L. Spires-Jones, R. Pitstick, G.A. Carlson, and B.T. Hyman. 2009. Tangle-bearing neurons survive despite disruption of membrane integrity in a mouse model of tauopathy. *J. Neuropathol. Exp. Neurol.* 68: 757–761. https://doi.org/10.1097/NEN.0b013e3181a9fc66

de Calignon, A., L.M. Fox, R. Pitstick, G.A. Carlson, B.J. Bacskai, T.L. Spires-Jones, and B.T. Hyman. 2010. Caspase activation precedes and leads to tangles. *Nature.* 464:1201–1204. https://doi.org/10.1038/nature08890

Elmore, M.R., A.R. Najafi, M.A. Koike, N.N. Dagher, E.E. Spangenberg, R.A. Rice, M. Kitazawa, B. Matusow, H. Nguyen, B.L. West, and K.N. Green. 2014. Colony-stimulating factor 1 receptor signaling is necessary for microglia viability, unmasking a microglia progenitor cell in the adult brain. *Neuron.* 82:380–397. https://doi.org/10.1016/j.neuron.2014.02.040

Erny, D., A.L. Hrabě de Angelis, D. Jaitin, P. Wieghofer, O. Staszewski, E. David, H. Keren-Shaul, T. Mahlakoiv, K. Jakobshagen, T. Buch, et al. 2015. Host microbiota constantly control maturation and function of microglia in the CNS. *Nat. Neurosci.* 18:965–977. https://doi.org/10.1038/nn.4030

Gale, S.C., L. Gao, C. Mikacenic, S.M. Coyle, N. Rafaels, T. Murray Dudenkov, J.H. Madenspacher, D.W. Draper, W. Ge, J.J. Aloor, et al. 2014. APOε4 is associated with enhanced in vivo innate immune responses in human subjects. *J. Allergy Clin. Immunol.* 134:127–134. https://doi.org/10.1016/j.jaci.2014.01.032

Hesdorffer, C.S., and D.L. Longo. 2015. Drug-induced megaloblastic anemia. *N. Engl. J. Med.* 373:1649–1658. https://doi.org/10.1056/NEJMra1508861

Josephs, K.A., J.L. Whitwell, Z. Ahmed, M.M. Shiung, S.D. Weigand, D.S. Knopman, B.F. Boeve, J.E. Parisi, R.C. Petersen, D.W. Dickson, and C.R. Jack Jr. 2008. β-amyloid burden is not associated with rates of brain atrophy. *Ann. Neurol.* 63:204–212. https://doi.org/10.1002/ana.21223

Kitazawa, M., S. Oddo, T.R. Yamasaki, K.N. Green, and F.M. LaFerla. 2005. Lipopolysaccharide-induced inflammation exacerbates tau pathology by a cyclin-dependent kinase 5-mediated pathway in a transgenic model of Alzheimer's disease. *J. Neurosci.* 25:8843–8853. https://doi.org/10.1523/JNEUROSCI.2868-05.2005

Krasemann, S., C. Madore, R. Cialic, C. Baufeld, N. Calcagno, R. El Fatimy, L. Beckers, E. O'Loughlin, Y. Xu, Z. Fanek, et al. 2017. The TREM2-APOE pathway drives the transcriptional phenotype of dysfunctional microglia in neurodegenerative diseases. *Immunity.* 47:566–581.e9. https://doi.org/10.1016/j.immuni.2017.08.008

Kuchibhotla, K.V., S. Wegmann, K.J. Kopeikina, J. Hawkes, N. Rudinskiy, M.L. Andermann, T.L. Spires-Jones, B.J. Bacskai, and B.T. Hyman. 2014. Neurofibrillary tangle-bearing neurons are functionally integrated in cortical circuits in vivo. *Proc. Natl. Acad. Sci. USA.* 111:510–514. https://doi.org/10.1073/pnas.1318807111

Leyns, C.E.G., J.D. Ulrich, M.B. Finn, F.R. Stewart, L.J. Koscal, J. Remolina Serrano, G.O. Robinson, E. Anderson, M. Colonna, and D.M. Holtzman. 2017. TREM2 deficiency attenuates neuroinflammation and protects against neurodegeneration in a mouse model of tauopathy. *Proc. Natl. Acad. Sci. USA.* 114:11524–11529. https://doi.org/10.1073/pnas.1710311114

Li, Y., L. Liu, S.W. Barger, and W.S. Griffin. 2003. Interleukin-1 mediates pathological effects of microglia on tau phosphorylation and on synaptophysin synthesis in cortical neurons through a p38-MAPK pathway. *J. Neurosci.* 23:1605–1611. https://doi.org/10.1523/JNEUROSCI.23-05-01605.2003

Luo, J., F. Elwood, M. Britschgi, S. Villeda, H. Zhang, Z. Ding, L. Zhu, H. Alabsi, R. Getachew, R. Narasimhan, et al. 2013. Colony-stimulating factor 1 receptor (CSF1R) signaling in injured neurons facilitates protection and survival. *J. Exp. Med.* 210:157–172. https://doi.org/10.1084/jem.20120412

Nandi, S., S. Gokhan, X.M. Dai, S. Wei, G. Enikolopov, H. Lin, M.F. Mehler, and E.R. Stanley. 2012. The CSF-1 receptor ligands IL-34 and CSF-1 exhibit distinct developmental brain expression patterns and regulate neural progenitor cell maintenance and maturation. *Dev. Biol.* 367: 100–113. https://doi.org/10.1016/j.ydbio.2012.03.026

Pimenova, A.A., T. Raj, and A.M. Goate. 2018. Untangling genetic risk for Alzheimer's disease. *Biol. Psychiatry.* 83:300–310. https://doi.org/10.1016/j.biopsych.2017.05.014

Shi, Y., and D.M. Holtzman. 2018. Interplay between innate immunity and Alzheimer disease: APOE and TREM2 in the spotlight. *Nat. Rev. Immunol.* 18:759–772. https://doi.org/10.1038/s41577-018-0051-1

Shi, Y., K. Yamada, S.A. Liddelow, S.T. Smith, L. Zhao, W. Luo, R.M. Tsai, S. Spina, L.T. Grinberg, J.C. Rojas, et al. Alzheimer's Disease Neuroimaging Initiative. 2017. ApoE4 markedly exacerbates tau-mediated neurodegeneration in a mouse model of tauopathy. *Nature.* 549:523–527. https://doi.org/10.1038/nature24016

Sluijter, M., T.C. van der Sluis, P.A. van der Velden, M. Versluis, B.L. West, S.H. van der Burg, and T. van Hall. 2014. Inhibition of CSF-1R supports T-cell mediated melanoma therapy. *PLoS One.* 9:e104230. https://doi.org/10.1371/journal.pone.0104230

Thion, M.S., D. Low, A. Silvin, J. Chen, P. Grisel, J. Schulte-Schrepping, R. Blecher, T. Ulas, P. Squarzoni, G. Hoeffel, et al. 2018. Microbiome influences prenatal and adult microglia in a sex-specific manner. *Cell.* 172:500–516.e16. https://doi.org/10.1016/j.cell.2017.11.042

Vitek, M.P., C.M. Brown, and C.A. Colton. 2009. APOE genotype-specific differences in the innate immune response. *Neurobiol. Aging.* 30:1350–1360. https://doi.org/10.1016/j.neurobiolaging.2007.11.014

Wang, Y., O. Berezovska, and S. Fedoroff. 1999. Expression of colony stimulating factor-1 receptor (CSF-1R) by CNS neurons in mice. *J. Neurosci. Res.* 57:616–632. https://doi.org/10.1002/(SICI)1097-4547(19990901)57:5<616::AID-JNR4>3.0.CO;2-E

Zhu, Y., E. Nwabuisi-Heath, S.B. Dumanis, L.M. Tai, C. Yu, G.W. Rebeck, and M.J. LaDu. 2012. APOE genotype alters glial activation and loss of synaptic markers in mice. *Glia.* 60:559–569. https://doi.org/10.1002/glia.22289

Supplemental material

Shi et al., https://doi.org/10.1084/jem.20190980

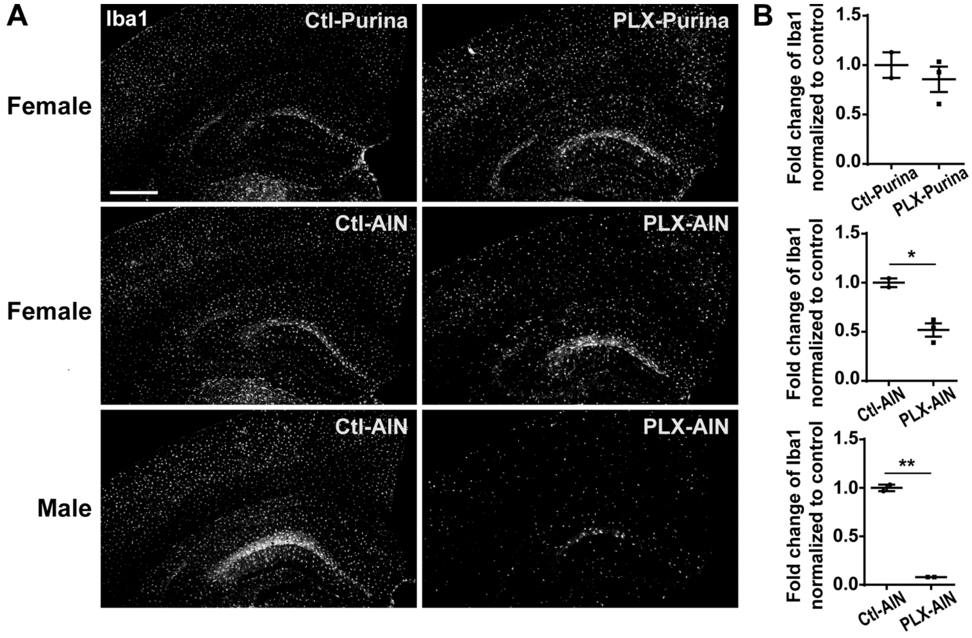

C

Female mice	Purina	AIN	Purina/AIN (%)
Drug incorporation rate in diet (%)	70	90	78
Average drug uptake per day μg (drug) / g (mouse weight)	23.7	29.6	80
Average plasma drug concentration (μg/ml)	134.3	299.7	45
Microglial depletion rate (%)	14	48	30

D

AIN chow	Female	Male	Female/Male (%)
Average drug uptake per day μg (drug) / g (mouse weight)	29.6	32	93
Average plasma drug concentration (μg/ml)	299.7	580	52
Microglial depletion rate (%)	48	92	52

Figure S1. **Mouse sex and chow formula impact the efficiency of microglial depletion by PLX3397. (A)** Iba1 staining images for 3–4-mo-old female or male TE4 mice treated with 300 mg/kg PLX3397 supplemented in either Purina-5053 or AIN-76A diet for 7 d (*n* = 2–3 mice per group). Scale bar = 500 µm for all images. **(B)** Quantification of Iba1-covered area in the hippocampus. **(C and D)** Effects of chow formula and sex on serum PLX3397 levels in relation to microglial depletion rate. Data are expressed as means ± SEM. One-way ANOVA with Tukey's post hoc test. *, P < 0.05; **, P < 0.01. The experiments in A and B were repeated three times.

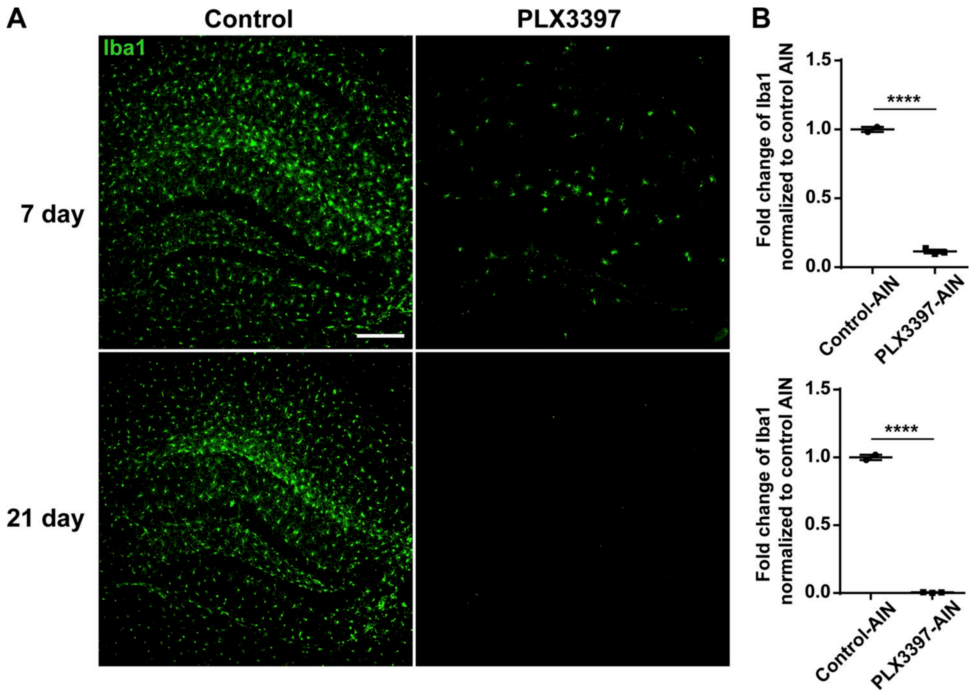

Figure S2. **PLX3397 supplemented in the AIN-76A diet at 400 mg/kg chow depletes microglia with high efficiency. (A)** Iba1 staining images for 5–6-mo-old male E4 mice treated with 400 mg/kg PLX3397 supplemented in the AIN-76A diet for 7 or 21 d (*n* = 2–3 mice per group). Scale bar = 200 µm for all images. **(B)** Quantification of Iba1-covered area in the hippocampus. Data are expressed as means ± SEM. One-way ANOVA with Tukey's post hoc test. ****, P < 0.0001. This characterization experiment was performed once.

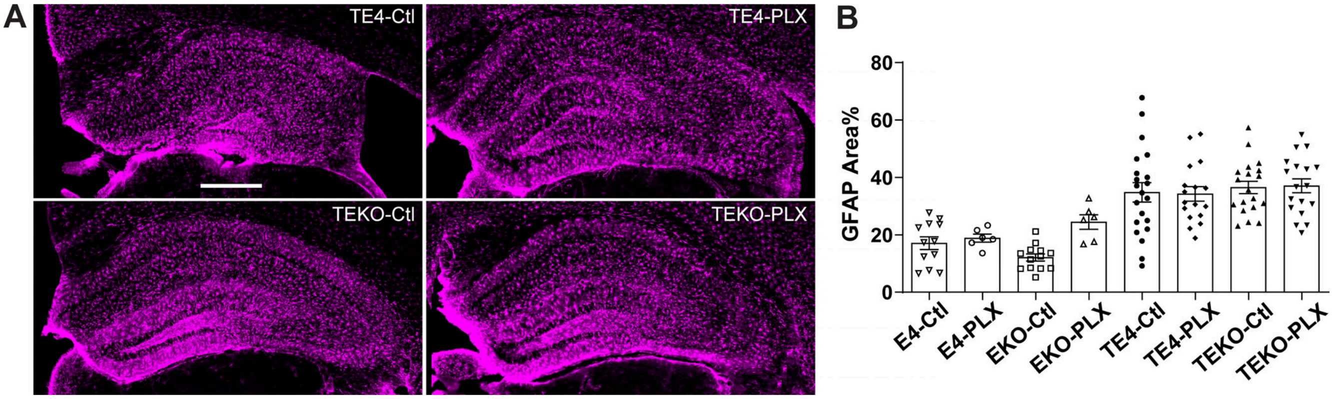

Figure S3. **PLX3397 treatment does not affect GFAP$^+$ astrocytes. (A)** Representative images of GFAP staining for 9.5-mo-old TE4 and TEKO mice treated with control (Ctx) or PLX3397-supplemented (PLX) chow. Scale bar = 500 µm for all images. **(B)** Quantification of GFAP-covered area in the hippocampus of all mice (TE4-Ctl: *n* = 21; TE4-PLX: *n* = 17; TEKO-Ctl: *n* = 19; TEKO-PLX: *n* = 18; E4-Ctl: *n* = 12; E4-PLX: *n* = 6; EKO-Ctl: *n* = 13; EKO-PLX: *n* = 6). Data are expressed as means ± SEM. One-way ANOVA with Tukey's post hoc test. The GFAP staining was performed once.

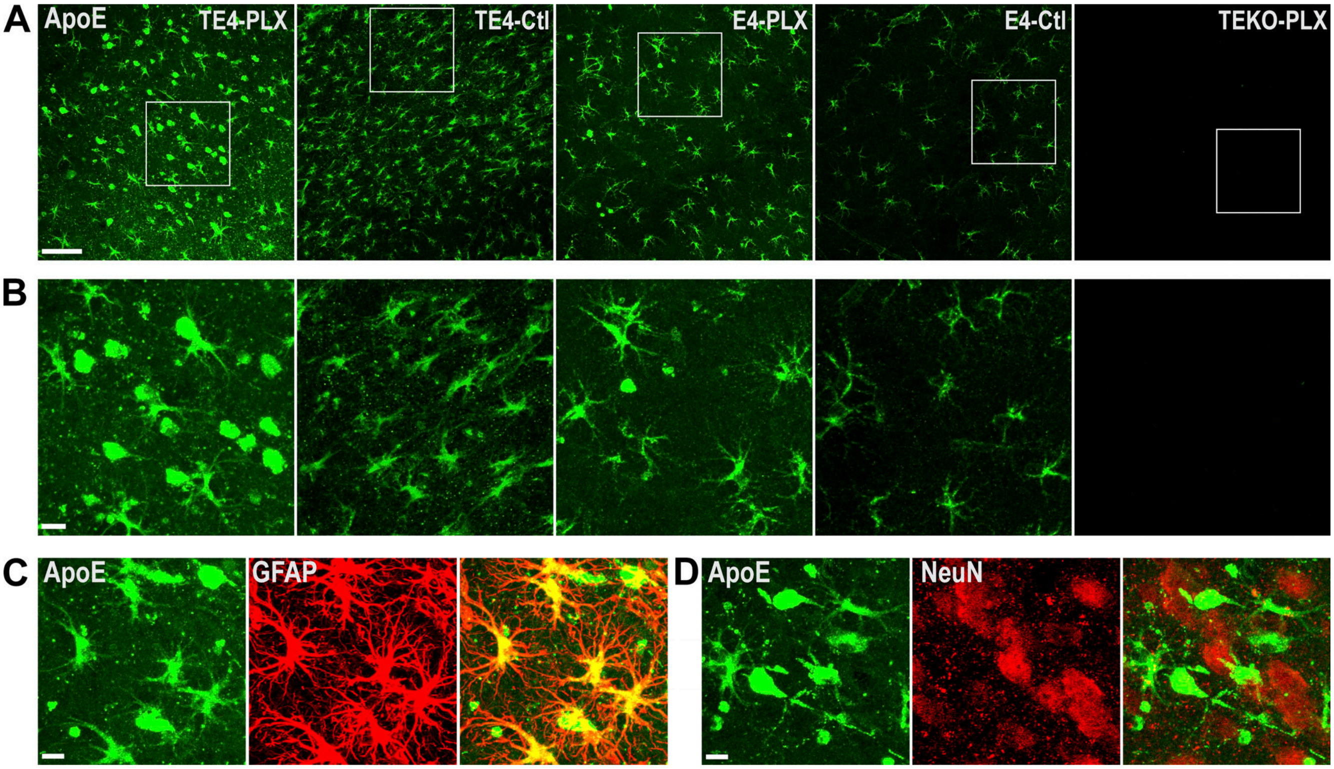

Figure S4. **ApoE is elevated in astrocytes and neurons in the piriform/entorhinal cortex of PLX3397-treated TE4 and E4 mice. (A)** Representative images of apoE staining in the piriform/entorhinal cortex of 9.5-mo-old TE4-PLX, TE4-Ctl, E4-PLX, E4-Ctl, and TEKO-PLX mice, respectively. Scale bar = 50 µm for all images. **(B)** Zoom-in of the selected area in A. Scale bar = 10 µm for all images. **(C)** Co-localization of apoE with GFAP$^+$ astrocytes in the piriform/entorhinal cortex of TE4-PLX mouse. Scale bar = 10 µm. **(D)** Non-co-localization between apoE and NeuN in the piriform/entorhinal cortex of TE4-PLX mouse. Scale bar = 10 µm. ApoE staining was repeated seven times using different antibodies.

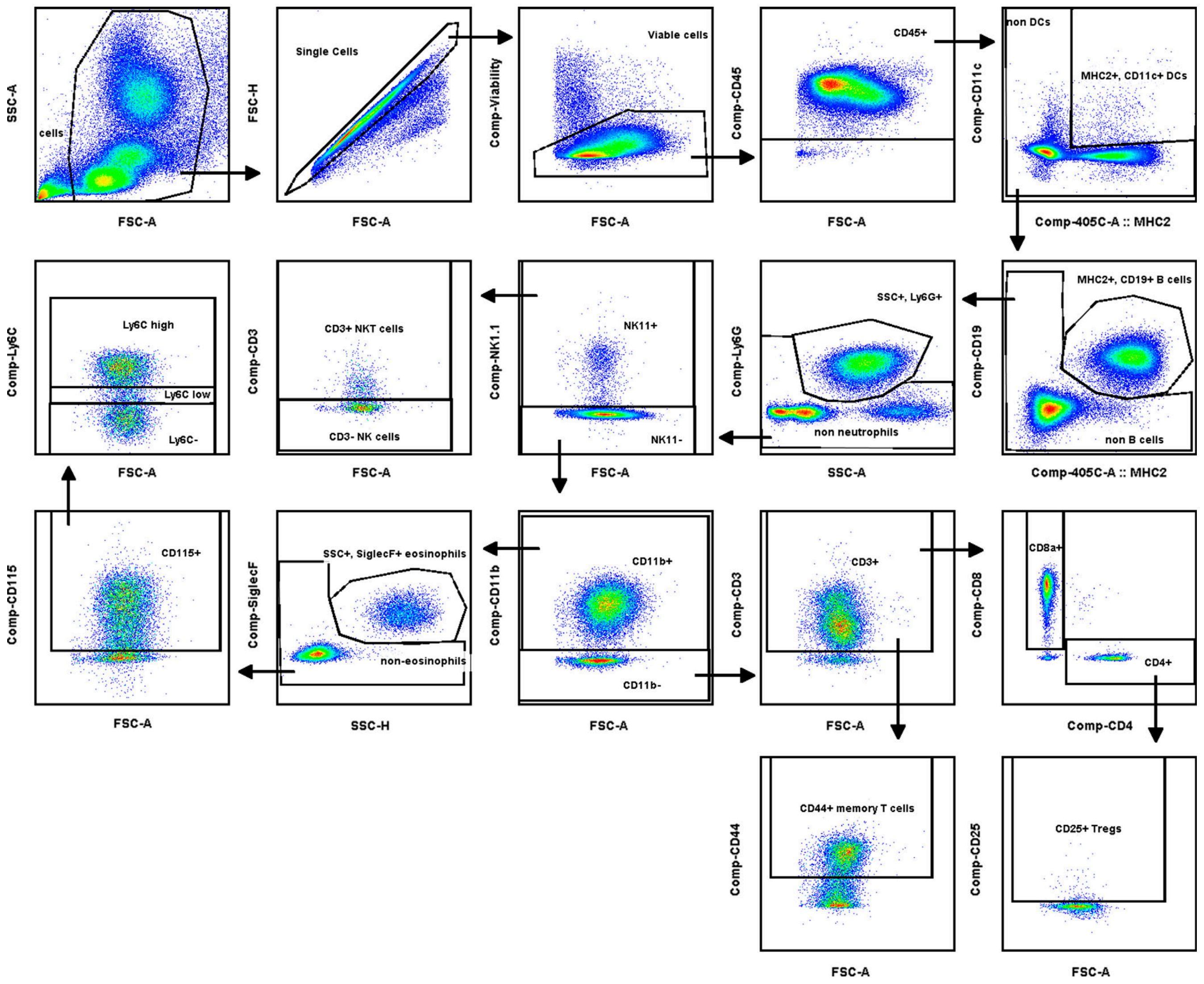

Figure S5. **Gating strategies for isolating blood cell types using flow cytometry.** Blood cells were sequentially gated through total cells, single cells, viable cells, and CD45$^+$ cells. From the CD45$^+$ gate, DCs were isolated as the MHC2$^+$CD11c$^+$ population. From the non-DC gate, B cells were isolated as the MHC2$^+$CD19$^+$ population. From the non-B cell gate, neutrophils were isolated as the SSC^{high}Ly6G$^+$ population. From the nonneutrophil gate, NK1.1$^+$ cells were isolated and further divided into CD3$^+$ NK T cells and CD3$^-$ NK cells. The NK1.1$^-$ gate was further separated into CD11b$^+$ and CD11b$^-$ gates. From the CD11b$^+$ gate, eosinophils were isolated as the SSC^{high}SiglecF$^+$ population. From the noneosinophil gate, monocytes were isolated as the CD115$^+$ population, which was further divided into Ly6C^{hi}, Ly6C^{lo}, and Ly6C$^-$ populations. From the CD11b$^-$ gate, T cells were isolated as the CD3$^+$ population, which was further separated into CD4$^+$ and CD8$^+$ T cells, or CD44$^+$ memory T cells. From the CD4$^+$ T cell gate, T reg cells were isolated as the CD25$^+$ population. SSC-A, side scatter area; FSC-A, forward scatter area; SSC-H, side scatter height.